ROBOTIC ULTRASOUND TOMOGRAPHY AND COLLABORATIVE CONTROL

by
Kevin Michael Gilboy

A thesis submitted to Johns Hopkins University in conformity with the requirements for the degree of Master of Science in Engineering

Baltimore, Maryland
May, 2020

Abstract

Ultrasound computed tomography (USCT) offers quantitative anatomical tissue characterization for cancer detection, and has shown similar diagnostic power to MRI on ex vivo prostate tissue. While most USCT research and commercial development has focused on submerging target anatomy in a transducer-lined cylindrical water-tank, this approach is not practical for imaging deep anatomy like the prostate and an alternative acquisition system using aligned abdominal and endolumenal ultrasound probes is required. This work outlines a clinical workflow, calibration scheme, and motion framework for an innovative dual-robotic USCT acquisition system specific to in vivo prostate imaging — one arm wielding a linear abdominal probe, the other wielding a linear transrectal ultrasound (TRUS) probe. After a three-way calibration, the robotic system works to autonomously keep the abdominal probe collinear with the physician-rotated TRUS probe using a hybrid force-position convex contour tracking scheme, while impedance control enforces its gentle contact with the patient's pubic region for capturing the transmission ultrasound slices needed for limited-angle tomographic reconstruction. TRUS rotation was induced by joystick control for precision during testing, however collaborative control via admittance control of hand forces presents a useful workflow option to the physician. An improved robot admittance control algorithm for transparent collaborative control utilizing Kalman filtering was developed and verified to smooth robot hand guidance. Such an improvement additionally has important implications for generally alleviating ultrasonographer musculoskeletal strain through cooperatively controlled robots. The ultimate dual-robotic USCT

system proved repeatable and sufficiently accurate for tomography based on pelvic phantom testing. Future steps in system verification and validation are discussed, as is incorporation into feasibility studies to test the potential and utility of the system for future prostate malignancy diagnosis and staging in vivo.

Co-Advisors: Dr. Emad Boctor, Dr. Russell Taylor

Acknowledgements

I would like to express my deepest appreciation to my co-advisors, Prof. Emad Boctor and Prof. Russell Taylor, for their mentorship and enthusiastic support during my thesis journey. I admire your dedication and field expertise, and the experience I have gained through our interactions has proven invaluable. I would also like to thank Dr. Mahya Shahbazi for her control theory and filtering mentorship throughout my research. I additionally would like to express gratitude to Prof. Mehran Armand for his loaning of a second UR5 robot for my experiments.

I would like to extend my thanks to my fellow members of Prof. Boctor's MUSIIC Lab. In particular, I would like to thank Yixuan Yu, who was a close collaborator, co-author on a pending paper submission on dual-robotic ultrasound tomography, and will be assisting with that work moving forward. I would also like to thank Tian Xie and Baichuan Jiang, who frequently heard my updates at weekly lab meetings and provided great feedback. Additionally, I would like to thank Dr. Fereshteh Aalimifar, Rodolfo Finocchi, and Ting-Yun (Angel) Fang who are graduated members of the MUSIIC lab that set a solid foundation for my work in robotic ultrasound tomography and collaborative control.

I would like to thank the team at the National Institutes of Health (NIH) Clinical Center that provided clinical and engineering support for this work, namely Dr. Bradford Wood MD and Dr. Reza Monfaredi. While our interactions were limited in number, your guidance and critiques were important in shaping the direction of this thesis. I would also like to thank two of my clinical mentors, Dr. Katarzyna Macura MD and Dr. Sarah Murthi MD, for

providing valuable end-user feedback on parts of this work and helping shape the scope of future development. I would also like to acknowledge NSF CAREER grant #1653322 “Co-Robotic Ultrasound Sensing in Bioengineering” for its funding of our lab’s robot-assisted ultrasound research thrust.

I would like to thank my family and friends for their unwavering support throughout my time at Johns Hopkins University, without whom none of this would be possible. I am forever grateful to my parents for always being there for me, providing steadfast encouragement and advice throughout my life that has shaped me into who I am today. I am also appreciative to have lived only a few minutes from my older brother these past two years, who has given me valuable life advice as a previous graduate student himself and is always someone I can always count on. Lastly, I would like to express my sincerest appreciation of Anisha Gopu for her immeasurable love, patience, and support.

Table of Contents

Table of Tables

Table of Figures

Chapter 1

Introduction

Ultrasound (US) as a medical imaging modality has long been heralded for its ability to provide rapid diagnostic imaging results with cheap, portable equipment and without the use of harmful ionizing energy [1]. A conventional US scan is performed by an ultrasonographer, who holds a probe against a patient after applying acoustic coupling gel. In pulse-echo mode, US energy is transmitted by the probe, and reflected back by changing acoustic impedances at tissue interfaces that cause impedance mismatch. The strength of this mismatch, size of the tissue boundary, and angle of US wave interaction, all contribute to alterations of the US energy and direction when it is reflected back to the probe [1]. These changes can be calculated and visually rendered, often as a B-mode image, by an US machine for clinical guidance [2].

US has traditionally been a popular choice for point-of-care preliminary diagnostics and interventions that require real-time visual feedback [3]. However, US is often not the gold standard when it comes to final diagnosis as CT and MRI provide much greater diagnostic accuracy [4]. This is because pulse-echo US is not inherently quantitative, has limited resolution at large depths, often cannot see isoechoic nor anechoic lesions, and is unable to accurately visualize targets in the presence of bone or anisotropic structures like needles [5, 6]. There has been a large breadth of research in improving traditional US

scanning methods to attenuate these disadvantages while maintaining the logistical benefits of US. One exciting field is US computed tomography (USCT), which uses multiple US slices to reconstruct quantitative speed-of-sound (SoS) representations of anatomy including echopoor regions [7]. Often, US has been enhanced through probe-wielding robots that aid in performing computer-integrated procedures like catheter tracking during insertion using piezoelectric elements [8], trauma assessment [9], whole-leg venous imaging [10], and visually guided biopsies using tracked anatomical movement through speckle decorrelation [11]. The pairing of robotics with US has also ushered in novel imaging paradigms such as synthetic tracked aperture US (STRATUS) imaging for improved resolution at depth, which is difficult to perform by hand [12]. These applications are usually supported by an underlying real-time software platform such as the Computer Integrated Surgical Systems and Technology (CISST) library and Surgical Assistant Workstation (SAW) packages [13] which are both utilized in this thesis. The trend of US enhancement, by incorporating auxiliary technological platforms with improved image processing, offers a promising realm of new scanning modalities that may improve US clinical diagnostic power.

1.1 Thesis Statement

A complete dual-robotic USCT system and workflow for in-vivo prostate cancer screening, enabled by a hybrid force-position robot motion framework and improved calibration results, and enhanced by an observer/estimator force filtering scheme allowing transparent hand-over-hand robotic probe control.

1.2 Prostate Cancer Imaging

Prostate cancer is the second leading non-cutaneous cancer and the fifth leading cause of cancer death globally for males in 2018 [14]. The modern diagnosis pathway usually first involves a combination of blood testing for prostate specific antigen (PSA) and B-Mode transrectal US (TRUS) scanning, as the combination of both has been shown to increase diagnostic accuracy versus either method used standalone. If there is a heightened concern for cancer, a multiparametric MRI follows [15]. MRI is often used in fusion with real-time TRUS data to localize malignancies for targeted biopsy, as well as stage them using the Gleason scale. While MRI is the de facto gold standard in prostate cancer diagnosis [4], it is usually costly and schedule-limited.

This raises the question if the initial TRUS procedure can be improved to enhance the sensitivity and specificity of cancer detection, allowing more definitive diagnostic conclusions before an MRI is needed. The usage of B-Mode TRUS in prostate cancer screening has been well studied, and only has a 50%-60% positive predictive value and approximately 6% detection rate due to undetectable isoechoic or echopoor lesions [16]. Due to the diagnostic limitations of pulse-echo, B-Mode US imaging, a different US scanning modality must be considered.

1.3 Ultrasound Computed Tomography

USCT is an imaging modality that allows quantitative tissue characterization via tomographic reconstruction of US slices, and has recently become popular due to enabling technological advancements in the field. In addition to producing a visual image, time-of-flight data collected during USCT allows calculation of an attenuation and SoS mapping for the target anatomy at any depth. Studies have shown these mappings to correlate well with tissue type in prostate biopsy samples [17]. Most relevantly, [18] showed that SoS

mappings generated by USCT on ex vivo prostate tissue correlates well with MRI-based pathology deduction.

Hardware and image reconstruction techniques for USCT have steadily improved since the debut of the system in the 1970s. Recent research and commercial development in USCT have mainly utilized transducer-lined cylindrical water-tanks for breast imaging. Two notable systems include the SoftVue by Delphinus [19] and QTScan by QT [20], which require the patient to lie on a specially designed table that has a cutout to the water-tank in which the patient submerges her breast for scanning. The latter system by QT was approved as a clinical-grade scanner by the FDA in 2017 [21] and has achieved success in transmission USCT breast imaging with comparable, and potentially superior, breast density and mass identification results to mammography and tomosynthesis scans [22]. Their product and water-tank schematic are shown in Fig. 1.1a and Fig. 1.1b respectively.

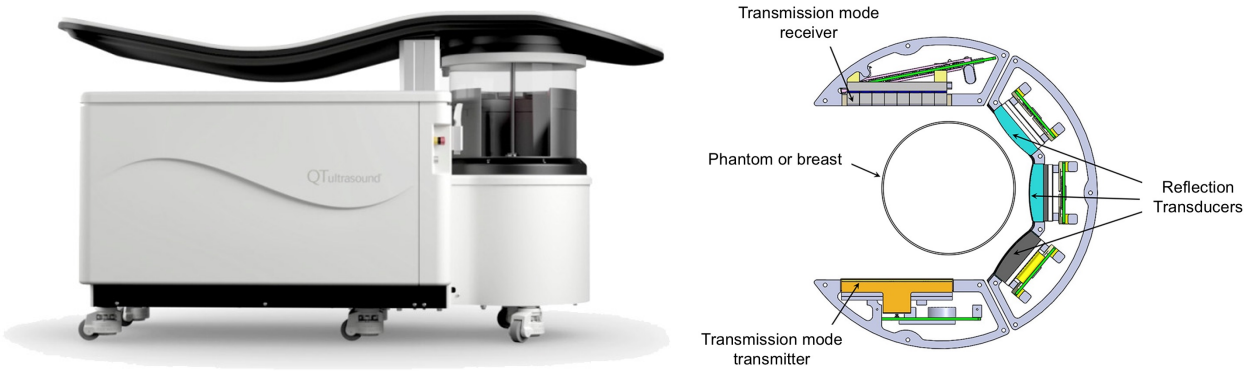

(a) (b)

Figure 1.1: (a) The QTScan system by QT for performing breast USCT via transmission US, clinically approved by the FDA in 2017 [21]. The system has shown results comparable to those of mammography and tomosynthesis [22]. Image from [20]. (b) An axial schematic of the QTScan water-tank, highlighting the utilized technology and breast placement. Image from [7].

QT has additionally shown the effectiveness of using inverse scattering to image a cadaver knee [23] and whole body piglet [24] immersed in their scanner tank. However, the authors at QT recognize the practical difficulties of in vivo, whole body scanning, and suggest the need for sedation and anesthesia. While it is easy to stably submerge a distal

appendage in a water-tank, imaging deep human anatomy in vivo presents an unsolved technical challenge. A novel US slice acquisition system is needed for prostate imaging.

1.4 Dual-Robotic Ultrasound Tomography

Dual-robotic US scanning approaches were largely pioneered by Dr. Fereshteh Aalamifar and other members of the Medical US Imaging and Intervention Collaboration (MUSIIC) lab at Johns Hopkins University, with which I am affiliated. Among other contributions, Dr. Aalimifar's dissertation [25] outlined a potential approach to non-specific USCT via transmission US utilizing two robotic arms wielding algorithmically aligned US probes: one for Tx and one for Rx. In general, a dual-robotic approach to USCT circumvents the need for anatomical submersion in a water-tank and thereby alleviates the sizing constraints of what can be imaged. She and her team built a dual-robotic rig from 80/20 T-slot Aluminum, and designed adapters to allow each robot to hold a linear abdominal probe. Her setup is shown in Fig. 1.2 below.

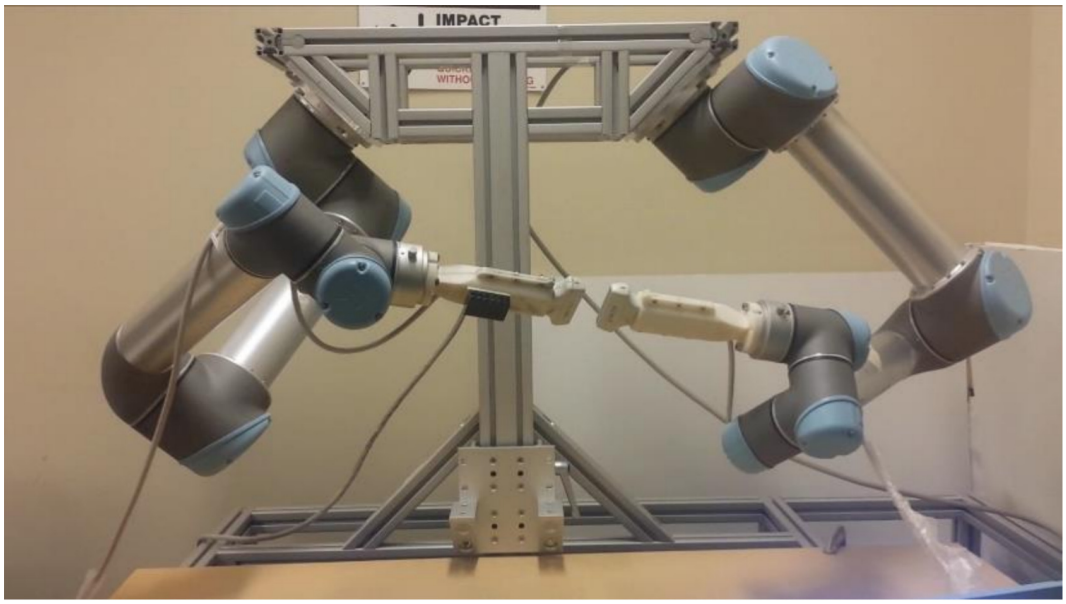

Figure 1.2: Figure from [25] showing the dual-robotic transmission USCT setup and feasibility test performed by Dr. Aalamifar. As one arm was manually commanded to move about the workspace through a GUI, the other arm autonomously servoed to align itself and maintain a constant distance between the probes.

After performing a three-way calibration to determine all system frame relations, she demonstrated the ability of her system to autonomously align one probe to be collinear with a manually commanded one in-air, while enforcing a constant distance between them. Dr. Aalimifar's limited preliminary implementation itself is not a suitable system for in vivo use, since it is not conducive for a specific clinical application nor does it consider automated patient-probe contact enforcement for anatomical slice acquisition. Additionally, the software was written in MATLAB to command sequential Cartesian positions to the robots, which has suboptimal speed compared to a faster, compiled implementation that commands Cartesian velocities at the update rate of the robot. However, Dr. Aalimifar's work serves as a useful proof-of-concept in demonstrating the feasibility of dual-robotic USCT. Her approach and calibration methods serve as an important motivator and starting point for this thesis.

1.5 Co-Robotic Ultrasound

Work by Rodolfo Finocchi, a Master's student in the MUSIIC lab, in hand-over-hand guidance for robotically-held US probes is also relevant to robotic USCT systems since some form of physician collaborative control is needed for the workflow. Rodolfo's thesis was primarily motivated to reduce ultrasonographer physical exertion during scanning, thereby alleviating musculoskeletal issues that they experience as a result of the repetitive microtrauma they incur over their career [26]. He also extended this work to include virtual fixtures for stable STRATUS imaging in collaboration with Dr. Haichong Kai Zhang [12]. His setup is shown in Fig. 1.3 below.

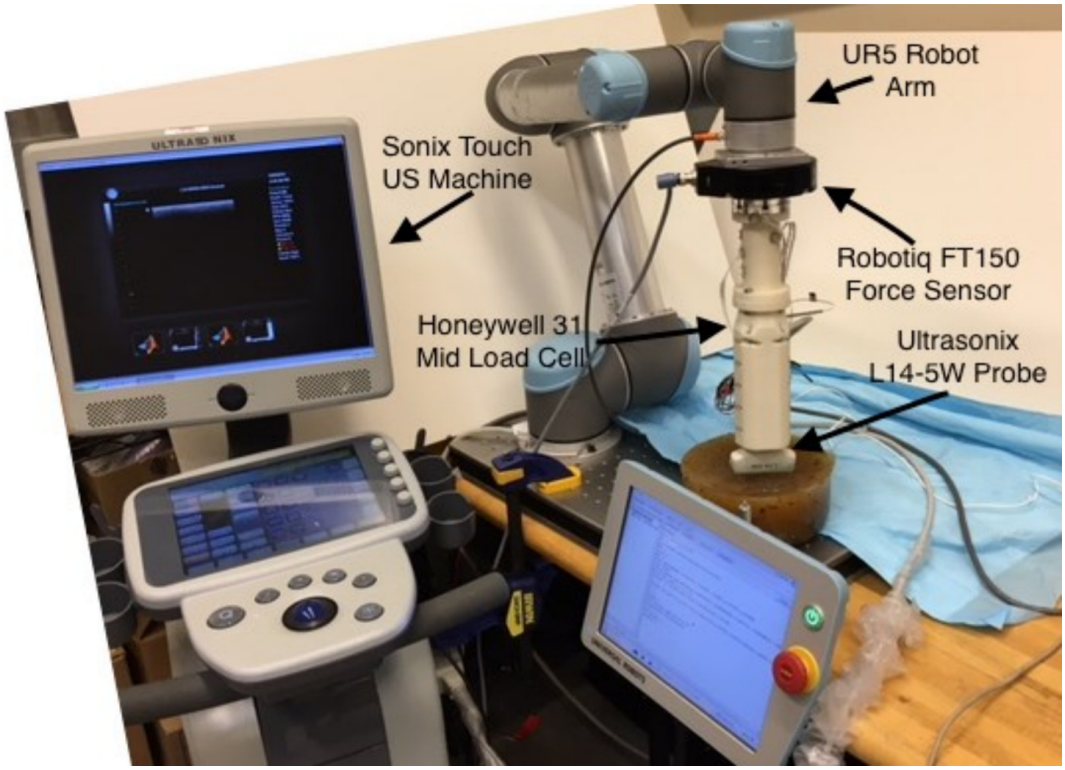

Figure 1.3: Figure from [26] showing Rodolfo's experimental setup and components.

In addition to traditional force admittance control of the form $\vec{v} = k\vec{f}$, he presented the use of a 1€ low-pass filter for force smoothing in an effort to improve the transparency of hand-guidance. Additionally, he proposed an impedance control algorithm for automated surface contact force exertion and tracking on flat surfaces. While Rodolfo's user study showed a decrease in ultrasonographer exertion, further transparency improvement could likely be made through advanced filtering methods such as observer/estimator schemes since hand trajectories are likely predicable and have a relatively low frequency component. Additionally, his software was written in MATLAB, which has suboptimal speed compared to a faster, compiled implementation, which may enhance transparency. His preliminary work in admittance control was influential to the direction of this thesis.

1.6 Summary of Contributions

The main goal of this thesis is to make important strides toward a clinically-usable dual-robotic USCT system for in vivo prostate imaging. This is accomplished through the following specific contributions of this thesis:

- Implemented a dual-robotic USCT system and workflow for in vivo prostate imaging through use of a joystick controlled endoluminal TRUS probe and autonomously servoed external linear probe.
- Developed and analyzed a hybrid force/position control algorithm and robot motion framework for concurrent probe alignment, gentle probe contact, and convex contour tracking of a patient's pubic region as demonstrated on a pelvic phantom.
- Performed and analyzed a three-way calibration of the dual-robotic setup similar to [25], but attained an improved calibration result.
- Validated the existence of an acoustic window through the prostate for USCT via transmission US imaging.
- Proposed an overall system validation method and several new features to guide future development and testing in the field of dual-robotic USCT for prostate imaging.
- Improved the transparency of robot collaborative control through the use of Kalman filtering to reduce force/torque noise by observing and predicting hand trajectories, and a near real-time C++ CISST/SAW implementation.
- Developed useful SAW components for a Robotiq-FT150 force/torque sensor (TCP/IP), Variense force sensor (RS-232), Honeywell load cell (ADC converted to RS-232), and analog joystick (ADC converted to RS-232).

1.7 Thesis Overview

In this chapter, the clinical problem of accurate prostate cancer screening has been motivated and alternative screening modalities have been explored. USCT presents promising diagnostic ability for prostate cancer, however it cannot be performed with current commercial systems.

In Chapter 2, the primary thesis contribution of a dual-robotic USCT system for prostate imaging is discussed. The chapter includes the hardware/software setup, calibration procedures, robot motion framework, and preliminary results of the system. The focus here is heavily on the implementation side and developing a robust workflow, as performing USCT reconstruction will be a logical and critical next step.

In Chapter 3, the secondary thesis contribution of improved force filtering for hand-over-hand control, as motivated by the tomography workflow and ultrasonographer ergonomics, is discussed. The chapter includes the hardware/software setup, filtering methodologies, and results of the system.

In Chapter 4, a general discussion and summary of the research and the overall proposed system is provided. The chapter includes the limitations, unaddressed considerations, future steps, and implications of the current work before ultimately concluding.

Chapter 2

Ultrasound Tomography System for Prostate Imaging

Ultrasound computed tomography (USCT) of the prostate for cancer diagnosis and staging was motivated in Chapter 1, with preliminary research showing similar diagnostic power between USCT and MRI on ex vivo tissue [18]. It was suggested that existing water-tank USCT systems are not conducive to imaging deep anatomy like the prostate, and therefore an alternative system and workflow was needed. Dr. Aalimifar took strides in this direction for her dissertation work [25]. Notably, she (1) performed USCT of a prostate phantom using two linear abdominal probes screwed into linear stages that were manually aligned, (2) built a dual-robot rig and demonstrated probe alignment for USCT in-air in non-real-time, and (3) proposed the use of a single-robot setup for prostate USCT, by having one of the probes be a physician controlled endolumenal TRUS probe. The goal of this chapter is to develop upon her third idea, providing the details and an implementation of a dual-robotic approach to specific to in vivo prostate USCT that could be used for future clinical testing.

In this chapter, we present an implemented dual-robotic system specifically for USCT of the prostate, including the clinical workflow, hardware, calibration, motion framework,

and results on a pelvic phantom. Parts of this chapter are pending acceptance to the MICCAI 2020 conference at the time of this writing. Yixuan Wu, a coauthor of the pending MICCAI submission, contributed to most US-related aspects of this project including B-mode parameter tuning, hardware setup for USCT slice acquisition, and system alignment verification in a water-tank. Our progress is rooted in the research of Dr. Fereshteh Aalimifar who developed a dual-robotic setup prototype and the necessary calibration schemes for general USCT procedures, as well as the concept of applying a robotic system to prostate imaging [25].

2.1 Proposed Workflow for Dual-Robotic Prostate USCT

The proposed clinical workflow uses two robots for element-wise transmission US slice acquisition and eventual tomographic reconstruction of the prostate: one to steadily hold a TRUS probe endolumenally while allowing manually induced movement along and about the insertional axis (2-DoF), and one to hold a linear abdominal probe externally that autonomously servos (6-DoF) and tracks movement of the TRUS probe to maintain collinear line-of-sight between the probes and enforce gentle contact with the patient's pubic region. The manual guidance for the TRUS probe can either be done with collaborative physician guidance via admittance control of hand forces, or via joystick for enhanced precision control.

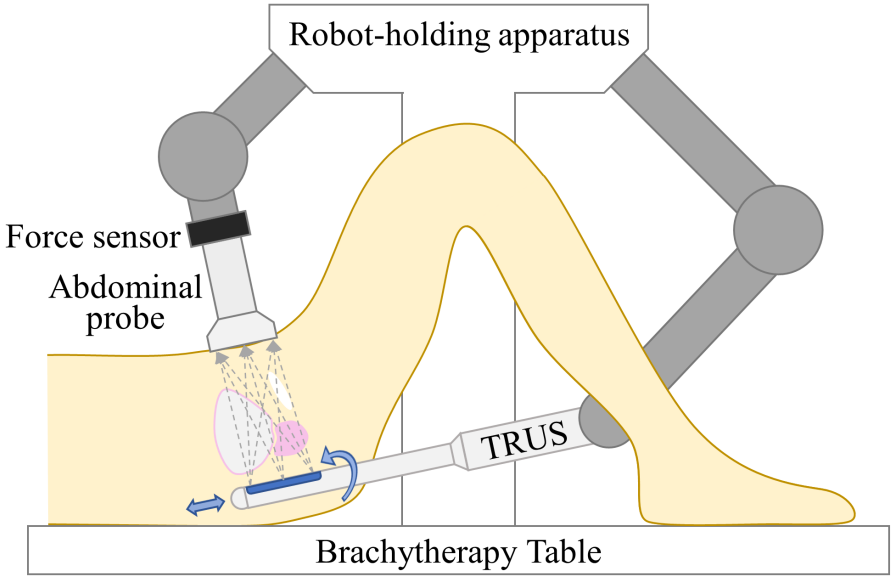

Figure 2.1: General approach to dual-robotic USCT. Important anatomy shown in addition to the prostate (pink) includes the bladder (pink outline) which may contain air and the pubic bone (white) which may obfuscate the view of US transmission.

The clinical workflow is (1) the patient (sedated, as is common for TRUS procedures) lies on a conventional brachytherapy table surrounded by the two robot arms, (2) the physician uses manual collaborative control guidance to insert the robotically-held TRUS probe then applies generous amounts of coupling gel to the pelvic region, (3) the software begins, and the robotically-held abdominal probe is autonomously lowered onto the patient's pubic region in alignment with the TRUS probe, (4) the physician manipulates the 2-DoF TRUS probe while the abdominal probe follows, allowing for continuous US transmission slice acquisition.

In this scheme, the TRUS probe must be the Tx transducer since it is closer to the prostate allowing the prostate to be more insonated than if the prostate were closer to the Rx transducer, where the acoustic energy has been lessened due to scatter. Additionally, the TRUS probe was chosen to be the physician controlled element (master) while the abdominal probe is servoed autonomously (slave). This decision was made since every 2-DoF translation and rotation of the TRUS probe has a corresponding 6-DoF abdominal probe pose that maintains alignment. The inverse, having the 6-DoF abdominal probe

physician controlled, does not guarantee a corresponding 2-DoF TRUS pose without prior constraints imposed on motion of the abdominal probe. While geometrically convenient to make the TRUS probe the physician guided element, this is also reasonable from a safety and clinical liability perspective since the TRUS probe is the more intrusive element.

2.2 System Setup

2.2.1 Hardware and Coordinate Frames

Two Universal Robots UR5 6-DoF robots were opposingly mounted at 45° on a custom 80/20 T-slot frame as shown in Fig. 2.2, and controlled by a central compute that commanded velocities to the respective robots over Ethernet. The two robots were outfitted with custom 3D printed adapters, shown in Fig. 2.3, to hold the BPL9-5/55 linear TRUS and L14-5W/60 linear abdominal probes respectively. The abdominal probe holder was previously designed and 3D printed by Ting-Yun (Angel) Fang who used a clamshell design with mechanical fasteners to securely hold the probe [27]. Her design was based on a prior iteration by Rodolfo Finocchi [26]. The TRUS probe holder was designed and 3D printed by us for this work, and features a threaded base and cap to hold the probe in place while still allowing easy installation and removal. The robot holding the abdominal probe additionally had a 6-DoF Robotiq FT150 force/torque sensor which was used for enforcing probe contact against the patient's pubic region. In certain scenarios, the robot holding the TRUS probe could also have a force/torque sensor to allow physician hand guidance, however we opted to use a joystick for more precise control during testing. The TRUS probe was connected to an UltrasonixTouch machine which sent scanline triggers to the SonixDAQ US acquisition system to which the abdominal probe was connected. Synchronization logic was implemented on an FPGA to only transmit scanline triggers to the DAQ on and after the rising edge of a frame trigger so that US transmission acquisi-

tion always started capture with the first elements. The phantom used for algorithm testing was a CIRS 048A pelvic phantom that had distinct SoS changes between the prostate, bladder, pubic bone, and surrounding tissue.

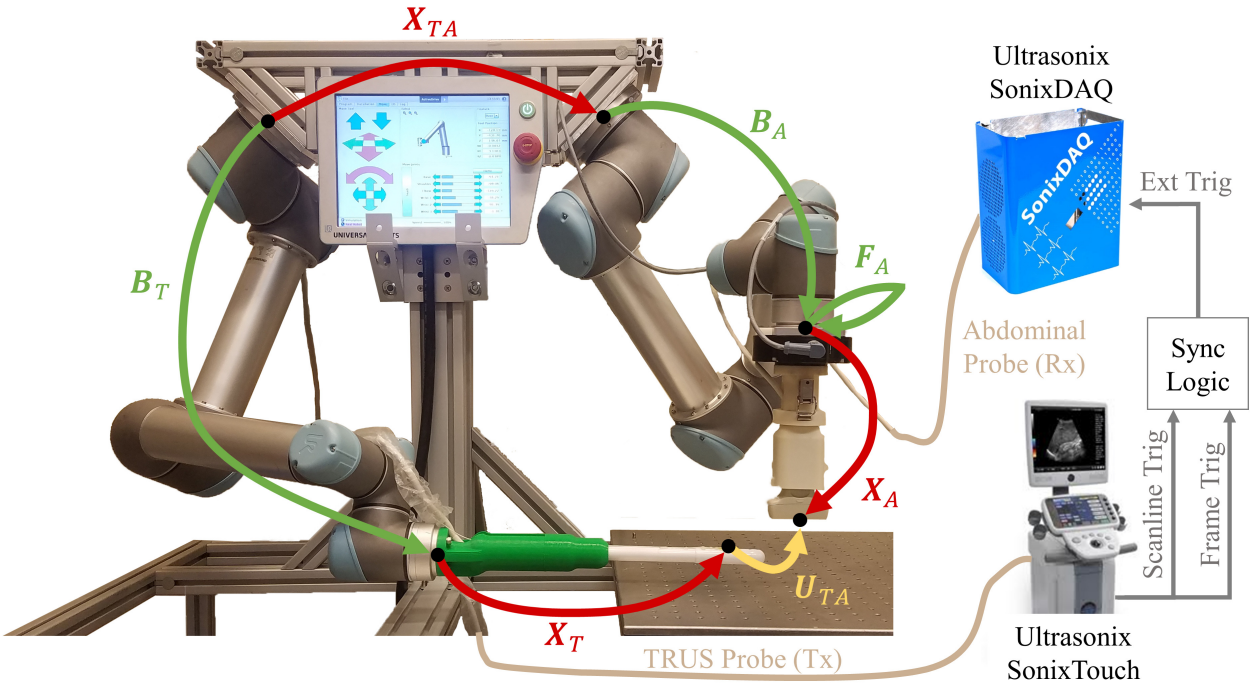

Figure 2.2: Experimental setup and frames, including two UR5 robots and their respective US systems tied together by a synchronized scanline trigger. Transformations in green are known, whereas those in red (named with X) are unknown but determinable through calibration.

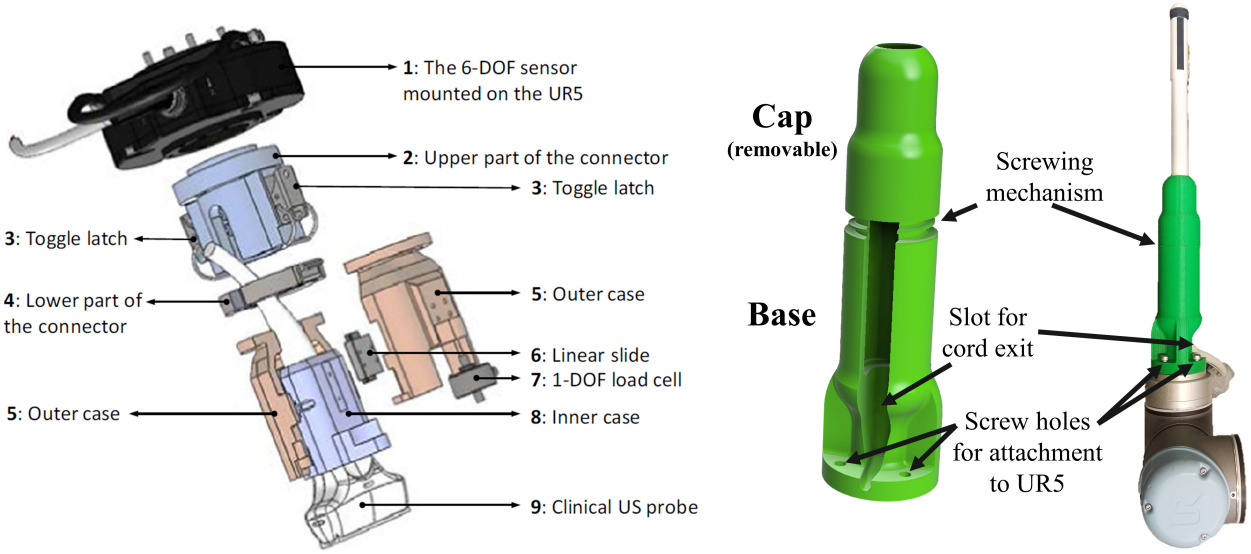

(a) (b)

Figure 2.3: (a) The L14-5W/60 linear abdominal probe holder developed and 3D printed for [27]. The clamshell design includes a load-cell to measure probe forces, which was not used for this work in favor of the larger 6-DoF Robotiq force/torque sensor affixed to the robot end-effector. (b) The BPL9-5/55 linear TRUS holder developed and 3D printed by us for this work. The design features a screwable cap for easy probe removal.

All relevant coordinate frame locations are shown in the above system diagram as black dots, with labelled and color-coded transformations to other coordinate frames. Green arrows represent known (or simply deducible) frame transformations, red arrows represent unknown but calibratable transformations, and the tan arrow represents a solvable transformation once all others have been calibrated.

The pose of the abdominal probe relative to its robot base can be written $B_A F_A X_A$, where $B_A \in SE(3)$ is the retrievable robot pose, $F_A \in SO(3)$ is the rotational transformation of the robot end-effector to the force/torque sensor, and $X_A \in SE(3)$ is the calibrated transformation to US image-space. Similarly, the pose of the TRUS probe relative to its robot base can be written $B_T X_T$. The transformation from the TRUS probe robot to the abdominal probe robot was called X_{TA}, allowing the relative orientation from the TRUS image-space to the abdominal image-space to be written as $U_{TA} = X_T^{-1} B_T^{-1} X_{TA} B_A F_A X_A$.

2.2.2 Software

All software was written in C++ using the Johns Hopkins University CISST/SAW libraries, compared to previous work that used MATLAB scripting. It was believed that a lower-level, compiled C++ implementation would provide inherent speedup benefits in addition to giving better hardware control to the implementer. We were able to have our run-loop operate around 125 Hz, the command limit of the UR5 robots. All software was developed within a Ubuntu 16.04 virtual machine for control and compatibility purposes.

The CISST library, intended for programming surgical systems, provided a pseudo real-time control architecture that abstracted most memory, communication, and scheduling considerations that are necessary for real-time software development. Most importantly, it had native support for accessing shared data in a way that prevents race conditions, which was very useful since this program relies on asynchronous, multitask execution and is therefore prone to data corruption. Among other things, it also provided classes and wrappers for matrix and frame calculations. The SAW packages, intended for interfacing CISST software with hardware through pseudo real-time tasks, provided an existing module for interfacing with UR5 robots over TCP/IP. Through the existing SAW component `sawUniversalRobot`, robot states could easily be read as CISST frames and new poses could be commanded as Cartesian/joint positions/velocities. Since our project additionally utilized hardware that was not yet wrapped into SAW components, we developed two additional SAW components that we hope to contribute as submodules to the SAW repository. They are:

- `sawRobotiqForceSensor`: This was used to communicate with the Robotiq FT150 force/torque sensor that was mounted on the abdominal probe UR5 robot. The sensor communicated over TCP/IP, sharing the same IP address as the UR5 robot but utilizing a separate port (63351). Through this interface, sensor packets were received by the computer socket at 20 Hz containing 100 Hz worth of force/torque data (i.e. every 50 ms, a packet would arrive with the past 5 force/torque readings).

The sensor additionally accepted a command of "`SET ZRO`" sent within a packet to initialize sensor-side rebiasing. The developed SAW component wrapped all functions for connecting to, receiving and parsing data from, and rebiasing the sensor.

- `sawJoystick`: This was used to communicate with the joystick used as optional input to the tomography system, allowing precise manual control of the TRUS probe robot. The joystick outputted its state as analog values, which were converted to a digital string using the ADC and microcontroller built into an Arduino Uno. The strings, sent over serial by the Arduino, were received by the computer at 9600 Hz. The developed SAW component wrapped all functions for connecting to, receiving and parsing data from, and rebiasing the joystick.

2.3 System Calibration

Four unknown frame transformations exist in the dual-robotic setup depicted in Fig. 2.2. Three of which could be calibrated for, while the fourth must be calculated once the other three have been solved. In this section, we outline the three-way calibration procedures performed, which were similar to those described in [25] and will only be briefly outlined.

2.3.1 Ultrasound Probe Calibrations

Two US probe calibrations had to be performed for X_A and X_T respectively to get the frame transformation from the robot end-effector to US image space. A conventional off-line cross-wire calibration was performed in a water-tank, where robot poses B_i were commanded and cross-wire locations in image-space p_i were collected through autonomous segmentation in captured US images. This information was used to solve a BXp calibra-

tion, in which X is solved as

$$\underset{X \in SE(3)}{\operatorname{argmin}} \sum_{i \neq j} \left\| B_i X p_i - B_j X p_j \right\|_2 \tag{2.1}$$

which was optimized through an iterative gradient descent procedure proposed in [28]. Sixty poses of each arm were collected, split into 54 training samples and 6 withheld test samples, to perform the X_A and X_T calibrations. Calibration accuracy was assessed by the mean and max of

$$E_i = \left\| B_i X p_i - \frac{1}{n} \sum\nolimits_j B_j X p_j \right\|_2 \tag{2.2}$$

which is the Euclidean distance between each calculated cross location and the average cross location.

2.3.2 Robot Calibration

Robot calibration of X_{TA} was performed by moving a cross-wire setup to multiple locations within the workspace, collecting robot poses B_i and cross-wire locations p_i in image-space for both robots. The cross-wire locations captured by the TRUS and abdominal probes, relative to the TRUS robot base, can be expressed as $B_T^i X_T p_T^i$ and $X_{TA} B_A^i F_A X_A p_A^i$ respectively. Solving for X_{TA} is a point-cloud registration problem of the form $A = XB$ that was solved with Horn's quaternion-based method [29]. Five non-collinear points were collected to perform the calibration. Calibration accuracy was assessed by the mean and max of

$$E_i = \left\| B_T^i X_T p_T^i - X_{TA} B_A^i F_A X_A p_A^i \right\|_2 \tag{2.3}$$

which is the Euclidean distance between the cross locations resolved by following the two independent kinematic chains originating from the TRUS robot base.

Since X_T and X_A were used in the calibration of X_{TA}, their errors propagate into the robot calibration. This could be alleviated in future work by using alternative calibration

methods such as a pivot calibration about a fixed point.

2.4 Robot Motion Framework

2.4.1 General Approach to TRUS Probe Velocity

TRUS probe movements were chosen to be joystick controlled, and were constrained about and along the insertional axis. This was done to prevent unintended off-axis motion of the intrusive probe which could cause patient harm. If the TRUS robot were equipped with a force/torque sensor, this constraint could be lifted in favor of detecting harmful probe forces with the sensor and reacting through closed-loop control. All user-induced joystick movements were converted into commanded velocities via the admittance control algorithm $\vec{v}_{trus} = k\vec{f}$, where $\vec{f}$ was the digitized positional readings from an analog joystick connected over serial using our `sawJoystick` component from Section 2.2.2.

2.4.2 General Approach to Abdominal Probe Velocity

Abdominal probe lateral velocities corresponding to TRUS probe movements were calculated using a form of hybrid force-position control, which generally aims to achieve desired end-effector force while constrained by desired robot tip pose in the presence of redundant DoFs [30]. This scheme was an ideal choice for our situation since abdominal probe alignment with the TRUS probe must be enforced while concurrently performing gentle, force-based convex contour tracking along the pubic region. As noted before, the abdominal probe is less constrained than the TRUS probe (6-DoF versus 2-DoF) making force-position control feasible. We implemented an interpretation of force-position control as a plane-axis intersection constraint coupled with impedance control. Commanded

abdominal robot velocities were the superposition of two velocity components

$$\vec{v}_{abdominal} = \vec{v}_{pose} + \vec{v}_{contact} \tag{2.4}$$

as shown in Fig. 2.4. Robot Cartesian velocity $\vec{v}_{pose}$ was needed to reorient the abdominal probe to be collinear with the TRUS while not having any velocity in the y-direction (toward the patient). The rotational component of the new probe pose was calculated using a goal transformation $U_{TA'}$ that defined what U_{TA} should approach for the two probes to be perfectly collinear. The translational component of the new probe location was calculated as the intersection of the TRUS line-of-sight vector with the plane formed by the abdominal probe transducer face. This plane-axis intersection constraint effectively nullified any probe y movement while still allowing the rotational movement necessary for probe alignment. The mathematical formulation of $\vec{v}_{pose}$ from these separate rotational and translational components is further described in the next section, Section 2.4.3. Robot Cartesian velocity $\vec{v}_{contact}$ was instead needed to produce y movement, enforcing probe coupling with the acoustic gel. It was calculated using impedance control of the form

$$\vec{v}_{contact} = K(F_D - F) - D(\dot{F}) \tag{2.5}$$

with stiffness K, damping D, desired force F_D which was only nonzero for contact force, and Kalman-smoothed force measurements F arriving from the Robotiq force/torque sensor using the `sawRobotiq` component described in Section 2.2.2. Kalman force/torque filtering is extensively discussed in Chapter 3.

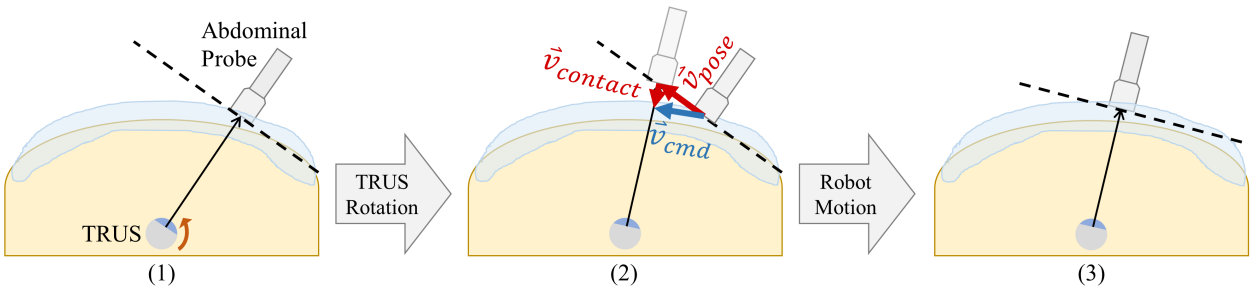

Figure 2.4: Proposed robot motion framework for abdominal probe alignment and contour tracking following a TRUS movement, shown on an axial pelvic slice: (1) Initial setup. (2) Two distinct velocity vectors arising from the plane-axis constraint and impedance control, and their superposition that was commanded to the robot. (3) Result of commanding velocities for a short duration.

This scheme ultimately aimed to keep the abdominal transducer aligned with the TRUS, while gently coupling it with the generously applied acoustic gel and without applying extraneous pressure to the patient (i.e. the skin should not "indent" under the applied force of the probe). It was effective for convex contour tracking, no matter the body habitus (i.e. curvature and fatty "compliance" of subcutaneous tissue), since the initial movement of the abdominal probe in response to a TRUS rotation is coplanar with its transducer face. Additionally, off-plane velocities toward/away from the patient are only commanded when the force/torque sensor signals that the probe is applying undesired pressure on the coupling gel. An upper bound was placed on the commanded velocities such that the probe could not escape the gel before the next velocity update occurred, which could have otherwise caused probe "palpating" and bubbles in the gel.

2.4.3 Formulation and Implementation of Abdominal Probe Velocity

The above robot motion framework calculated abdominal probe velocities after a TRUS probe movement as the superposition of a reorientation velocity ($\vec{v}_{pose}$) and gentle contact-seeking velocity ($\vec{v}_{pose}$). This process can be described mathematically through several steps. The equations below were simulated in MATLAB before being transcribed to a CISST implementation for the dual-robotic USCT system. An additional illustration of relevant frame transformations and parameters is provided below in Fig. 2.5 for convenience.

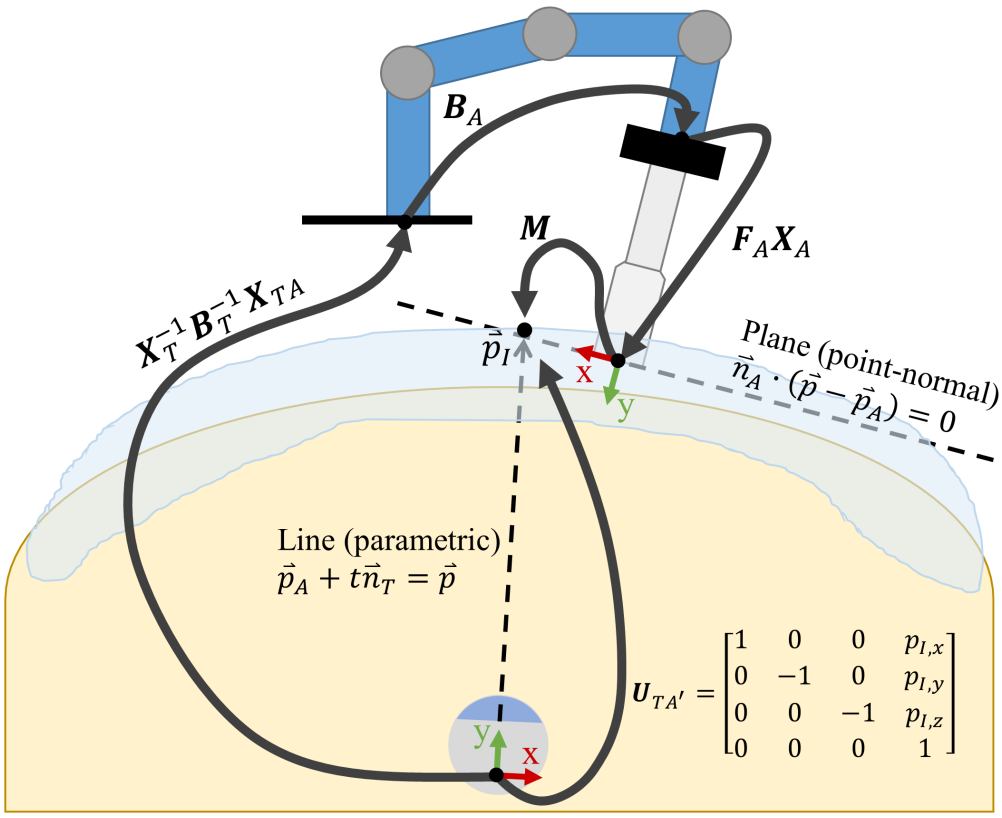

Figure 2.5: Axial slice of the pelvic phantom, illustrating both US probes and all coordinate frame transformations relevant when calculating an abdominal probe velocity based on a TRUS rotation.

Phase 1: Calculate $\vec{v}_{pose}$

1. **Calculate Plane-Axis Intersection:** We formulated $\vec{v}_{pose}$ to command the abdominal probe coplanar to its face (so that y-velocity toward the patient is not generated), while concurrently aligning with the TRUS probe. The desired position of the abdominal probe was calculated as the intersection of the TRUS probe's line-of-sight (represented by a line $\vec{n}_T$ with point $\vec{p}_T$) with the abdominal probe plane (represented by a normal vector $\vec{n}_A$ with point-on-the-plane $\vec{p_A}$). We considered everything relative to the TRUS probe frame for mathematical simplicity. Additionally, the y-axis was the pertinent axis since it runs in the direction of the transducer faces. The relevant components were calculated as

$$\vec{p}_A = translation(X_T^{-1} B_T^{-1} X_{TA} B_A F_A X_A) \tag{2.6}$$

$$\vec{n}_A = rotation(X_T^{-1} B_T^{-1} X_{TA} B_A F_A X_A) * \begin{bmatrix} 0 \\ 1 \\ 0 \end{bmatrix} \tag{2.7}$$

$$\vec{p}_T = \begin{bmatrix} 0 \\ 0 \\ 0 \end{bmatrix} \text{ (since relative to TRUS probe)} \tag{2.8}$$

$$\vec{n}_T = \begin{bmatrix} 0 \\ 1 \\ 0 \end{bmatrix} \text{ (since relative to TRUS probe)} \tag{2.9}$$

We made use of the common geometrical formulation for plane-axis intersection through t parameterization to find the point of intersection ($\vec{p}_I$) with respect to the TRUS probe

$$t = \frac{\vec{n}_A \cdot \vec{p}_A - \vec{n}_A \cdot \vec{p}_T}{\vec{n}_A \cdot \vec{n}_T} \tag{2.10}$$

$$\vec{p}_I = \begin{bmatrix} x_I \\ y_I \\ z_I \end{bmatrix} = \left[\vec{p}_T + t \odot \vec{n}_T \right] \tag{2.11}$$

2. **Use Plane-Axis Intersection to Find New Pose**: We formulated the pose of the abdominal probe located at $\vec{p}_I$ that also has orientation pointing toward the TRUS probe. The desired transformation from the TRUS to abdominal probe was written using homogeneous coordinates as

$$U_{TA'} = \begin{bmatrix} 1 & 0 & 0 & \\ 0 & -1 & 0 & \vec{p}_I \\ 0 & 0 & -1 & \\ 0 & 0 & 0 & 1 \end{bmatrix} \tag{2.12}$$

which constitutes a 180° rotation about the x-axis to make the probes face inward toward each other, coupled with a translation that keeps the abdominal probe face on the same plane. The desired abdominal probe pose relative to the current pose was written as

$$M = X_A^{-1} F_A^{-1} B_A^{-1} X_{TA}^{-1} B_T X_T U_{TA'} \tag{2.13}$$

which was simplified to the new desired pose of the abdominal probe robot

$$\widehat{B_A} = B_A F_A X_A M X_A^{-1} F_A^{-1} \tag{2.14}$$

3. **Calculate $\vec{v}_{pose}$ to Reach $\widehat{B_A}$**: While $\widehat{B_A}$ could be commanded as a new Cartesian position to the UR5 robot, we resolved it into a velocity ($\vec{v}_{pose}$) so that $\vec{v}_{contact}$ can be added to it in Phase 3 when calculating $\vec{v}_{abdominal}$. The Cartesian velocity $\vec{v}_{pose}$ was calculated by passing the rotational and translational components of $\widehat{B_A} B_A^{-1}$ into a PID loop for smoothing and scaling.

Phase 2: Calculate $\vec{v}_{contact}$

Contact velocity was simpler to calculate than the pose velocity from phase 1. Equation (2.5) was used to calculated $\vec{v}_{contact}$, with all desired torques set to zero and the only non-zero desired force set in the y-direction to enforce contact with the gel. This desired force was set to a low 3 N.

Phase 3: Calculate $\vec{v}_{abdominal}$

The resultant $\vec{v}_{abdominal}$, as previously outlined in equation (2.4), was calculated as the superposition of $\vec{v}_{pose}$ and $\vec{v}_{contact}$. Several safety checks were performed to clip large velocities, or even abort the procedure if a large force magnitude was detected. If $\vec{v}_{abdominal}$ was deemed reasonable, it was commanded as a Cartesian velocity to the UR5 holding the abdominal probe.

2.5 Results

2.5.1 System Calibration

Euclidean distances between cross locations and their centroid were calculated by equation (2.2) using withheld test data for X_A and X_T, resulting in $\overline{E} = 0.13mm \pm 0.08mm$,

$0.52mm \pm 0.30mm$ respectively, and $\max\{E\} = 0.26mm,\ 1.08mm$ respectively. Repeating calibration and testing with shuffled datasets yielded similar results. Euclidean distances between cross locations resolved in each arm were calculated by (2.3), resulting in $\overline{E} = 0.58mm \pm 0.32mm$ and $\max\{E\} = 1.01mm$.

These submillimeter individual calibrations, considering the repeatability of both robots (0.1 mm), likely propagate into an overall system accuracy within a few millimeters, which exceeds the accuracy reported by Dr. Aalimifar and is therefore acceptable for tomography by her proposed standard [25]. The accuracy difference between linear abdominal and TRUS probes should be noted, and is the result of the longer TRUS probe lever-arm and difficulty of maneuvering it into unique configurations within a water-tank.

2.5.2 Robot Motion Framework

Orientation and force data were collected while rotating the TRUS probe within the pelvic phantom such that the abdominal probe laterally traversed the pelvic region once. An axial projection of abdominal probe Cartesian positions and orientations on the phantom surface with respect to a stationary coordinate frame (defined as the initial frame of the TRUS probe) is shown in Fig. 2.6, where the probe is observed to smoothly trace a 2nd-degree polynomial approximation of the convex phantom pelvic region. The graph indicates that the abdominal probe successfully maintained collinearity with the TRUS probe during lateral traversal. It also shows subtle movement of the TRUS probe while rotating due to slight X_T calibration inaccuracy amplified over the length of the TRUS probe.

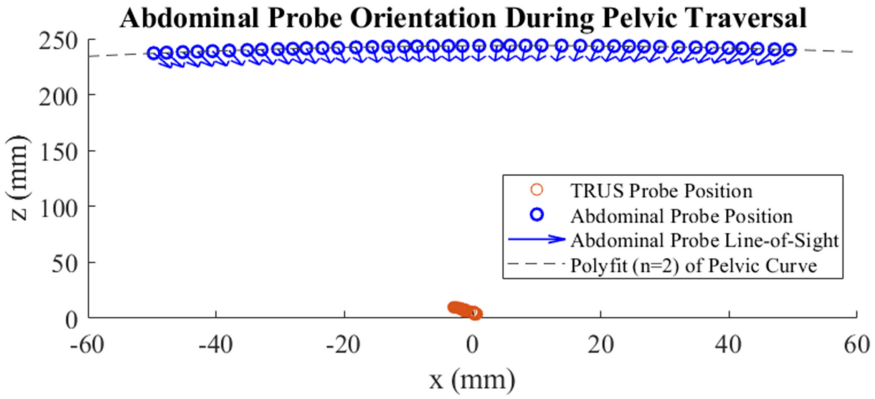

Figure 2.6: Abdominal probe Cartesian positions and orientations on the pubic region while rotating the TRUS probe, projected into 2-D and downsampled for clarity. Arrows show abdominal probe line-of-sight.

The detected force magnitudes during the traversal are shown in Fig. 2.7, and averaged $2.15N \pm 0.15N$. Detected torque magnitudes were negligible during this period, and averaged $0.07N \cdot m \pm 0.03N \cdot m$. The timeplot indicates that the abdominal probe maintained continuous contact with the acoustic coupling gel while tracing the pubic contour, and applied constant and gentle forces to the phantom without palpating. This emphasizes the stability of the proposed motion framework. Additionally, the abdominal probe was observed to "hover" on the generously applied gel pad during its traversal, as designed, without abraising, tugging, or indenting the phantom surface. This is desirable for patient comfort and air bubble avoidance, and is likely robust to varying pubic region curvatures and subcutaneous fat compliances across patients.

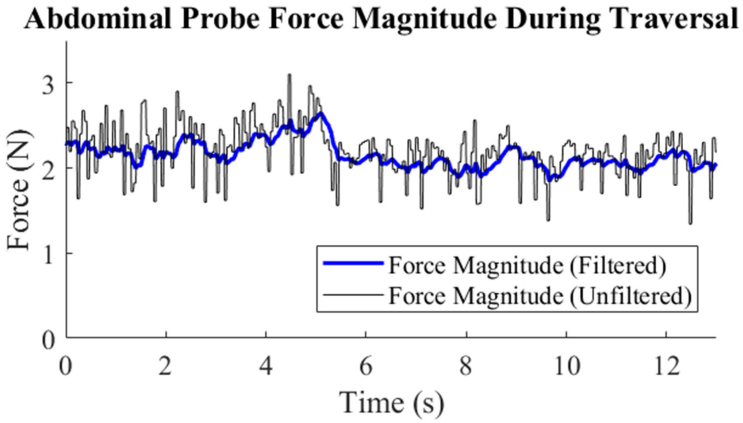

Figure 2.7: Abdominal probe force while performing the lateral pelvic traversal in Fig. 2.6.

2.5.3 Transmission US Verification

Three tests were performed to verify the ability of the dual-robotic system to collect transmission US slices of a pelvic phantom prostate using its novel rectum-to-abdomen approach. The tests encompassed potential imaging issues identified by our team and clinical mentors, including anatomical obfuscation, transmission distance, and acquisition angles. These tests were essential requisites for extending the system to collect true transmission US slices of the phantom prostate toward USCT reconstruction in the future.

First, we sought to verify qualitatively that the prostate can be viewed through an anatomical window that is neither obfuscated by the air-filled bladder nor dense pelvic bone when the abdominal and TRUS probes are held on the mid-sagittal plane facing toward each other. This was a primary concern of our team and clinical mentors, as transmission US cannot be conducted without a proper acoustic window. The manual overlay of two captured, opposing B-mode images is shown in Fig. 2.8 and shows the pubic bone, the shadow it casts, and the bladder. Clearly, a sufficient line-of-sight ("acoustic window") for transmission US through the prostate can be identified. It should be noted that the acoustic window is tilted slightly forward, suggesting that a prostate USCT procedure may require the probes to be slightly tilted forward as opposed to parallel with the examination table.

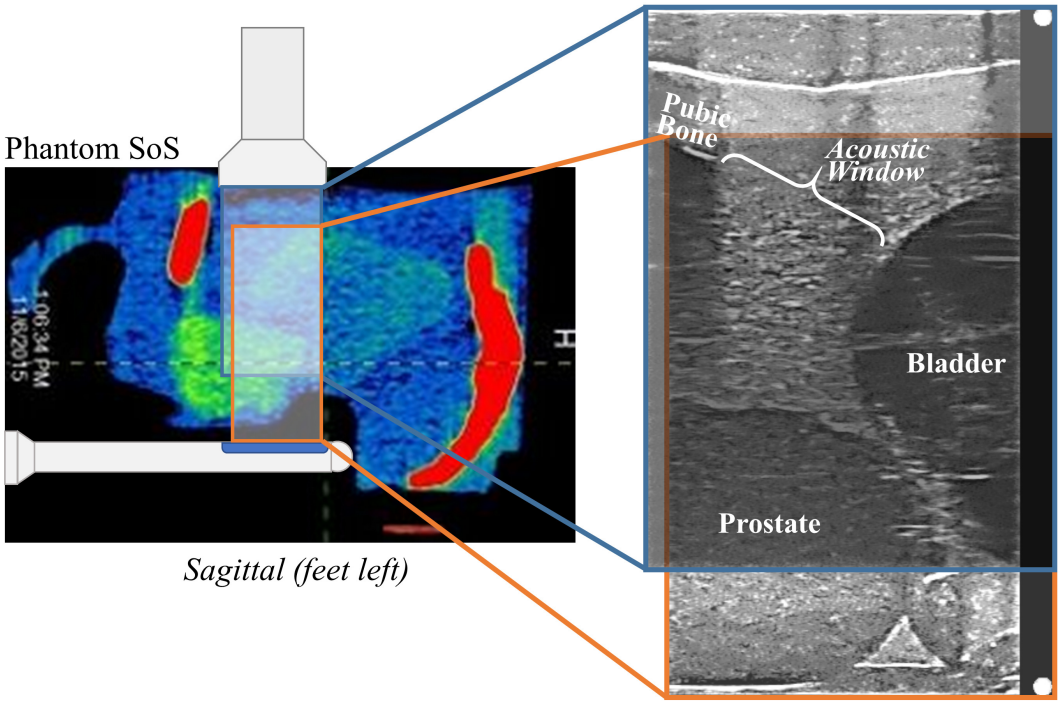

Figure 2.8: Overlay of B-mode images acquired by both probes showing an acoustic window for transmission US of the prostate.

Second, we sought to verify that the depth of the phantom (from rectum wall to pubic surface) is not too deep since it is the distance that the US energy must penetrate when travelling from the TRUS probe to abdominal probe. Based on the data collected for Fig. 2.6, there was between 9.1 to 9.5 inches of separation between the two probes as the abdominal probe traversed across the entire phantom pubic surface. While this seems adequate for a one-way propagation of US energy, our testing does not consider a larger body habitus and further quantitative signal attenuation testing is needed for verification.

Third, we sought to quantify the number of prostate slices that could be acquired with our phantom-based tomographic setup, as this determines the quality of USCT SoS mapping that can be reconstructed. As seen in Fig. 2.6, the phantom pelvic surface limited the TRUS probe to only rotate about 23.3° total, as any further rotation would cause the aligned abdominal probe to lose contact with the phantom due to the phantom's physical housing. Fortunately, the allowable TRUS rotation captured nearly all of the prostate, as proven through B-Mode visualization, which is encouraging for future testing with the

pelvic phantom. While the rotational accuracy of the UR5 wrist joint is unpublished, the internal 720 CPR motor encoder suggests a 0.5° precision, which would theoretically allow 46 prostate slices to be acquired within the pelvic phantom. It is difficult to deduce if this is sufficient for reconstruction, and further testing is needed for verification.

2.6 Discussion and Conclusion

The innovative dual-robotic setup, workflow, precise calibrations, and robot motion framework that we proposed is clinically feasible for US slice acquisition of the prostate toward tomographic reconstruction. It is difficult to quantify the overall system accuracy required for USCT since US transmission imaging of the in vivo prostate by these means has not been attempted before, however we believe that the submillimeter accuracy attained by our individual calibrations is sufficient for SoS mapping as per the results of Dr. Aalimifar [25]. This work also investigated and partially validated the anatomical feasibility of collecting transmission US slices through the prostate with a novel rectum-to-abdomen approach. Testing identified (1) a suitable acoustic window to the prostate that avoided bladder and pubic bone interference, (2) an acceptable depth for the US energy to propagate through assuming a non-obese patient, and (3) a quantification of collectable angles using the available pelvic phantom.

Future work should first focus on refining requirements for sufficient system validation and verification. In particular, the exact overall system accuracy and number of slices necessary for USCT should be deduced in collaboration with researchers focused on reconstruction methods. Second, relevant calibration test schemes should be implemented according to the requirements. For instance, the overall system in-plane and out-of-plane accuracy should be distinguished through water-tank testing and channel data analysis. Additionally, the distance that transmission US can propagate through while still being effective for USCT should be quantified, which is an important consideration for patients

with a large body habitus.

The main technical limitation of a dual-robotic USCT approach is the need for an accurate three-way calibration of the two probes and robots. Future work should include an improved active element calibration scheme for determination of X_A and X_T, as well as an alternative calibration scheme for X_{TA} that isolates it from errors propagated by X_A and X_T. We are additionally interested in a novel on-line calibration fine-tuning scheme for X_{TA}, in which the TRUS probe emits periodic pulses and the receiving abdominal probe, acting as a hydrophone, uses gradient descent guided motion to centralize itself directly within the TRUS probe's line-of-sight as a means for calibration.

It is likely beneficial to provide physicians with the ability to hand guide the TRUS probe through collaborative control (also called "cooperative control"), as opposed to with the joystick. Additionally, it may be clinically useful to provide them with the option to manually guide the abdominal probe (which would be constrained) while the TRUS is autonomously rotated. However, previous work on implementing admittance control for hand-over-hand US probe manipulation lacked the control transparency necessary for an interventional setting and an improved force/torque filtering approach is needed. Improved force/torque filtering would also improve the efficacy of the contact-seeking, impedance controlled velocity component of the proposed robot motion framework. Progress on transparent hand-over-hand control through enhanced filtering, additionally motivated by providing ultrasonographers with probe "power-steering" to alleviate occupation-related musculoskeletal issues, will be explored in the next chapter.

There is an abundance of future work for this robotic USCT system, not to mention potential advances in limited-angle tomographic reconstruction methods to build accurate SoS maps from the collected data. It is our ultimate hope that, when applied in a human trial, the slices collected by a refined dual-robotic USCT system will produce SoS mappings that improve prostate cancer diagnosis and staging.

Chapter 3

Transparent Hand-Over-Hand Control

The previous chapter motivated the desire for improved force/torque filtering within the proposed dual-robotic USCT imaging scheme. It would enable transparent probe hand guidance through admittance control, giving the operator more intuitive and intimate manipulation of the robot-held probe compared to a joystick, as well as improve contour tracking as performed through the impedance control scheme described in Section 2.4.1.

The realm of US robot applications is much larger than USCT as described in Section 1. Smoothed probe force/torque measurements through improved filtering would have widespread implications for the entirety of robot-assisted interventional US. For this reason, we sought to re-scope our clinical motivation to be more extensive than just improving the USCT system.

US guided procedures typically require an ultrasonographer to hold an US probe against a patient in static, contorted positions for long periods of time while also applying large forces [31]. As a result of this repetitive microtrauma, 63%-91% of ultrasonographers develop occupation-related musculoskeletal disorders compared to only about 13%-22% of the general population [32]. Our vision, building upon the previous work of [26, 27], was to provide ultrasonographers with US probe “power-steering” via a collaboratively controlled, hand guidable robot that can be maneuvered to a point-of-interest and then

released, at which the robot does all the strenuous holding on the ultrasonographers behalf. While we now focused on improving ultrasonographer ergonomics during routine scans, the developed force/torque filtering mechanism for providing smooth hand-over-hand control could subsequently be ported to our USCT system.

In this chapter, we present and discuss an observer/estimator-based filtering and admittance control approach for improving the perceived motion transparency of a hand guided US robot. Parts of this work were performed as activities for the Johns Hopkins University Computer Integrated Surgery II class, and text has been utilized from the final class report. Our progress is rooted in the research of Rodolfo Finocchi and Angel Fang who wrote a MATLAB script to perform 1€ low-pass filtering for force smoothing toward a hand guided US robot system. We used an identical robot setup and their 3D printed probe adapters, and sought to improve the transparency of the US robot motion since their system was observed to feel unnatural and difficult to maneuver.

3.1 System Setup

3.1.1 Hardware

The hardware setup was as shown in Fig. 3.1 below. A desktop computer was used to communicate with a UR5 6-DoF robot using TCP/IP on a private LAN. Through this connection, the computer received position, velocity, and force information while transmitting commanded velocities. The dual-force sensing, US probe wielding end-effector developed in [27] and used by our USCT experiments was also attached to the robot for this work. The system was designed and intended to use “dual-force” sensing since, in addition to the 6-DoF Robotiq FT-150 F/T sensor that measured applied hand forces, a second force sensor was included to discern forces applied by the probe to the patient or phantom. Two force sensors were available for this task: a 1-DoF Honeywell Model

31 mid-range load cell and a 3-DoF Variense FSE103 force sensor. Unfortunately, issues were found with both sensors and therefore contact compensation was not performed. However, the equations and procedure for including compensation in our admittance control loop is thoroughly described later in this section.

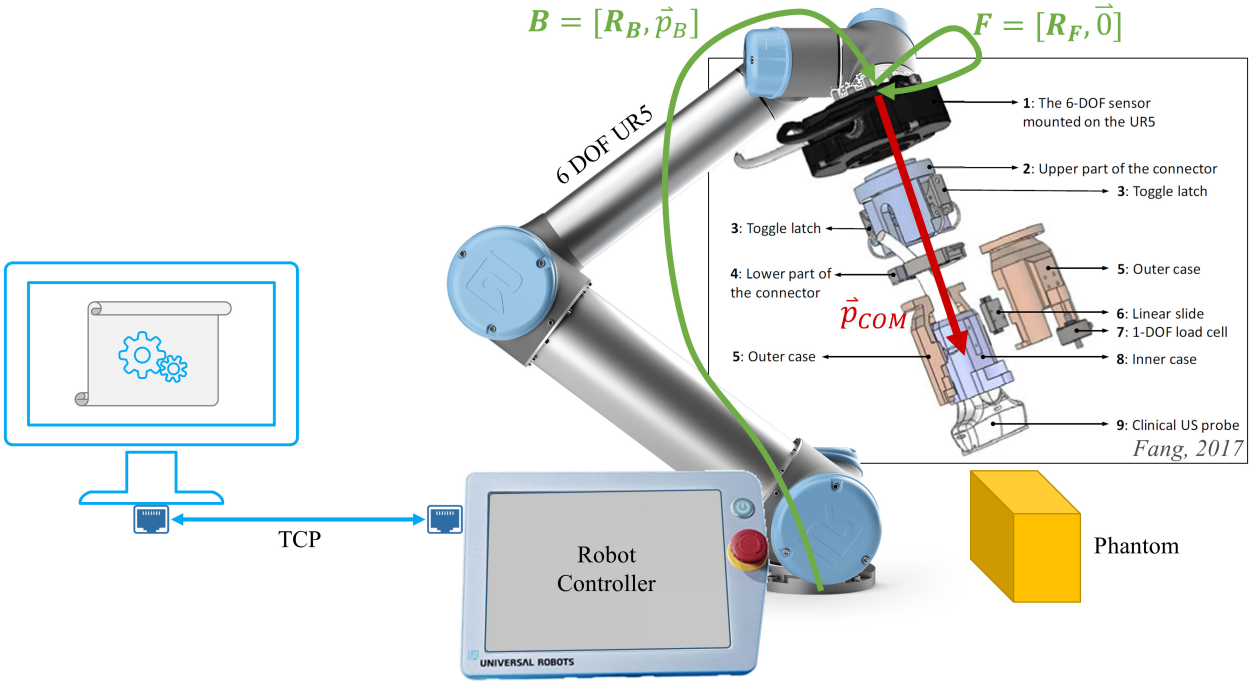

Figure 3.1: The experimental setup for this work, which includes a computer commanding a UR5 robot over TCP/IP as well as probe-holding end-effector developed by Fang [27] (figure inside the black border is from [27]). While a 1-DoF load cell is shown in the diagram, a 3-DoF force sensor was also tried in its place, however both produced unusable results. Transformations in green are known, whereas the red transformation to the probe center of mass is unknown.

All relevant coordinate frame locations are shown in the above system diagram, with labelled and color-coded transformations to other coordinate frames. Green arrows represent known (or simply deducible) frame transformations, while the red arrow represents an unknown but calibratable transformation.

3.1.2 Software

All software was written in C++ using the CISST/SAW libraries, compared to previous work that used a MATLAB client and robot-side server script for communicating move-

ment commands. It was believed that a lower-level, compiled C++ implementation would provide inherent speedup benefits in addition to giving better hardware control to the implementer. A C++ program that directly commanded the UR5 robot on its native TCP command port (30004) would also alleviate the need for an unoptimized, robot-side `.urp` file that spawns a server for receiving commands. We were able to have our run-loop operate at 125 Hz, the command limit of the UR5 robot. All software was developed within a Ubuntu 16.04 virtual machine for control and compatibility purposes.

Similar to the dual-robotic USCT implementation, the SAW component `sawUniversalRobot` was used for communicating with, and commanding, the UR5 robot. The `sawRobotiqForceSensor` component that we developed earlier was also used here for detecting hand forces. We also developed SAW components `sawVarienseForceSensor` and `sawHoneywellForceSensor` for the second force sensor meant to be included for isolating probe contact forces. However, as previously mentioned, the respective Variense and Honeywell force sensors were nonfunctional and therefore not included in the scope of this software implementation. A simplified flow diagram of all the component interactions is provided in Fig. 3.2.

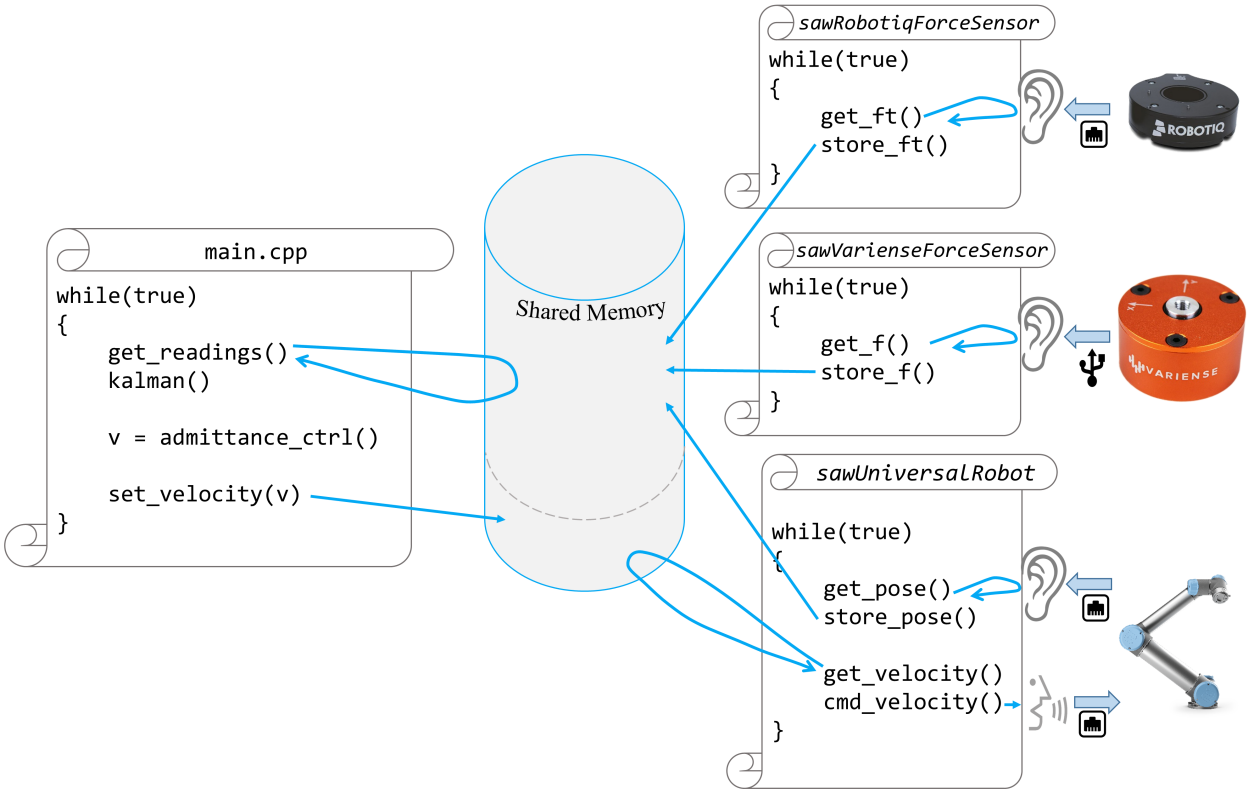

Figure 3.2: A simplified code flow diagram showing the asynchronous component listeners and `main.cpp` which performed the filtering, admittance control, and robot commanding.

3.2 Technical Approach

The general technical approach to the complete hand-over-hand control algorithm, from hardware interfacing to admittance control, will be described sequentially in the following subsections. A graphical overview of the dataflow is shown below, with each triangle representing a signal-manipulating functional component that will be described in a subsequent subsection.

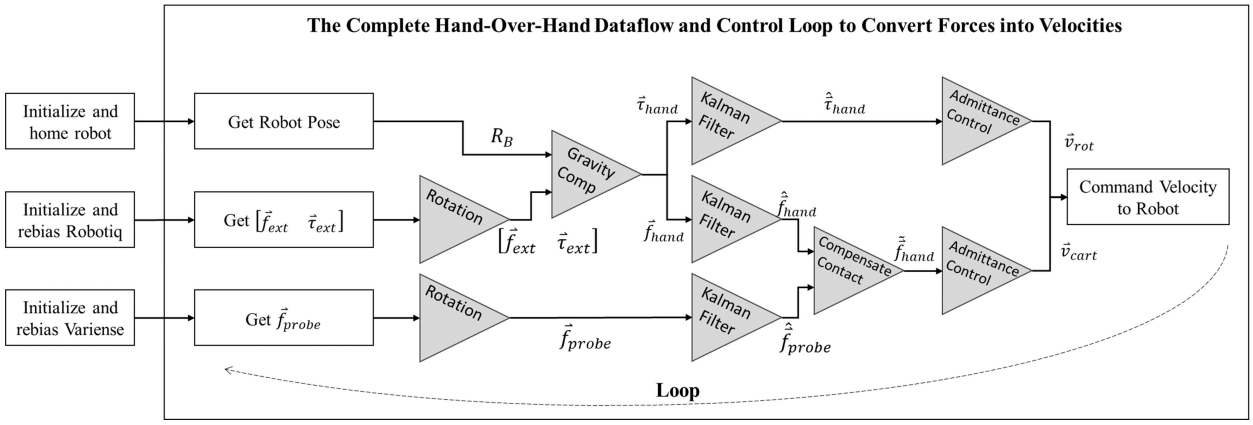

Figure 3.3: The overall dataflow and passage of signals for the implemented admittance control loop. After initialization, the loop includes frame transformations, gravity compensation, Kalman filtering, contact compensation, and admittance control. Each of these aspects are described in detail later in this section.

3.2.1 Force Alignment

Due to the orientation of the Robotiq force sensors with respect to the robot end-effector, a rotation matrix R_F was used to reorient the observed forces into the robot base frame. Since the sensor was rigidly fixed to the robot at a convenient angle, R_F could be determined by induction. This sensor was oriented with the z-axis coaxial to the robot base frame z-axis and the x/y axes rotated $\frac{\pi}{2}$ about the z-axis. From the base frame to the Robotiq, this resulted in the ZYX Euler angles $(\frac{\pi}{2}, 0, 0)$ and therefore rotation matrix

$$R_B = \begin{bmatrix} 0 & -1 & 0 \\ 1 & 0 & 0 \\ 0 & 0 & 1 \end{bmatrix} \tag{3.1}$$

3.2.2 Gravity Compensation

Gravity (tool weight) compensation was performed on each reading from the Robotiq 6-DoF force/torque sensor based on the robot's pose at that instant. This is because the reading of external forces from the Robotiq, $\vec{F}_{ext} \equiv \left[\vec{f}_{ext} \quad \vec{\tau}_{ext}\right]$, is a summation of the

forces caused by the operator's hand, $\vec{F}_{hand} \equiv \begin{bmatrix} \vec{f}_{hand} & \vec{\tau}_{hand} \end{bmatrix}$, and the forces induced from gravity acting upon the US probe and housing, $\vec{F}_{grav} \equiv \begin{bmatrix} \vec{f}_{grav} & \vec{\tau}_{grav} \end{bmatrix}$. Our goal was to solve for $\vec{F}_{hand}$ through the measurement of $\vec{F}_{ext}$ and prior analytical deduction of $\vec{F}_{grav}$:

$$\begin{bmatrix} \vec{f} \\ \vec{\tau} \end{bmatrix}_{hand} = \begin{bmatrix} \vec{f} \\ \vec{\tau} \end{bmatrix}_{ext} - \begin{bmatrix} \vec{f} \\ \vec{\tau} \end{bmatrix}_{grav} \tag{3.2}$$

Using the frames outlined in Fig. 3.1, equation (3.2) was rewritten expressing the measured gravitational force contribution as a function of robot pose

$$\begin{bmatrix} \vec{f} \\ \vec{\tau} \end{bmatrix}_{hand} = \begin{bmatrix} \vec{f} \\ \vec{\tau} \end{bmatrix}_{ext} - \left(\begin{bmatrix} R_B R_F & 0 \\ -R_B R_F \cdot sk(\vec{p}_{COM}) & R_B R_F \end{bmatrix} \begin{bmatrix} 0 \\ 0 \\ -mg \\ 0 \\ 0 \\ 0 \end{bmatrix} + \begin{bmatrix} 0 \\ 0 \\ -mg \\ 0 \\ 0 \\ 0 \end{bmatrix} \right) \tag{3.3}$$

where the second addition of the $-mg$ was meant to "undo" the sensor rebiasing and add in the expected amount of gravity contribution. This was the same equation used in [33]. Compensation requires knowledge or deduction of the weight contribution of the US probe and housing when in the vertical position ($-mg$), as well as the x and y center-of-mass coordinates ($\vec{p}_{COM}$) for the probe. Both of these quantities were unknown, and had to be analytically calculated from testing. We collected and averaged 1000 samples of force data for the robot oriented into 32 known static poses equally distributed around the workspace, orchestrated by a batch test script. Since there were no hand forces

applied during data collection, equation (3.3) simplified to

$$\left(\begin{bmatrix} R_B R_F & 0 \\ -R_B R_F \cdot sk(\vec{p}_{COM}) & R_B R_F \end{bmatrix} + I_{6\times 6} \right) \begin{bmatrix} 0 \\ 0 \\ -mg \\ 0 \\ 0 \\ 0 \end{bmatrix} = \begin{bmatrix} \vec{f} \\ \vec{\tau} \end{bmatrix}_{ext} \tag{3.4}$$

from which $-mg$ and $\vec{p}_{COM}$ were solved. Equation (3.4) was reduced to

$$\begin{bmatrix} \vdots \\ R_B^i R_F + I_{3\times 3} \\ \vdots \end{bmatrix} \begin{bmatrix} 0 \\ 0 \\ -mg \end{bmatrix} = \begin{bmatrix} \vdots \\ \vec{f}^{\,i} \\ \vdots \end{bmatrix}_{ext} \tag{3.5}$$

where i represents the *i-th* pose out of the 32 collected. This equation is in Ax=B form and was solved in a least-squares sense for $-mg$. Once $-mg$ was calculated, equation (3.4) was reduced to

$$-R_B R_F \cdot skew(\vec{p}_{COM}) \begin{bmatrix} 0 \\ 0 \\ -mg \end{bmatrix} = \begin{bmatrix} \vec{f} \end{bmatrix}_{ext} \tag{3.6}$$

which, using the definition of a skew-symmetric matrix and further simplification, was rearranged to

$$\begin{bmatrix} \vdots \\ R_B^i R_F \cdot (mg) I_{3\times 3} \\ \vdots \end{bmatrix} \begin{bmatrix} p_{COM,y} \\ -p_{COM,x} \\ 0 \end{bmatrix} = \begin{bmatrix} \vdots \\ \vec{f}^{\,i} \\ \vdots \end{bmatrix}_{ext} \tag{3.7}$$

which is also in Ax=B form and was solved in a least-squares sense for $p_{COM,x}$ and $p_{COM,y}$.

Once $-mg$, $p_{COM,x}$, and $p_{COM,y}$ were analytically calculated, they were plugged into (3.3) as part of the admittance control loop to convert a measured $\vec{F}_{ext}$ into the actual $\vec{F}_{hand}$.

3.2.3 Kalman Filtering

The Robotiq force sensor used in this project experienced a noise range of up to 2 N (± 1 N) and was the main "rate-limiting factor" of the admittance control loop since it sent packets at a speed up to 6.25X slower than the robot could be commanded. This is highlighted in Fig. 3.4, which shows that force packets arriving at 20 Hz severely limits the command rate of the robot operating at a potential 125 Hz (illustrated by the unfilled circles on the UR5 timeline). Providing slow and noisy input to an admittance control algorithm would produce unacceptable performance and therefore, a force/torque smoothing and interpolation scheme was needed for proper, transparent robot hand guidance.

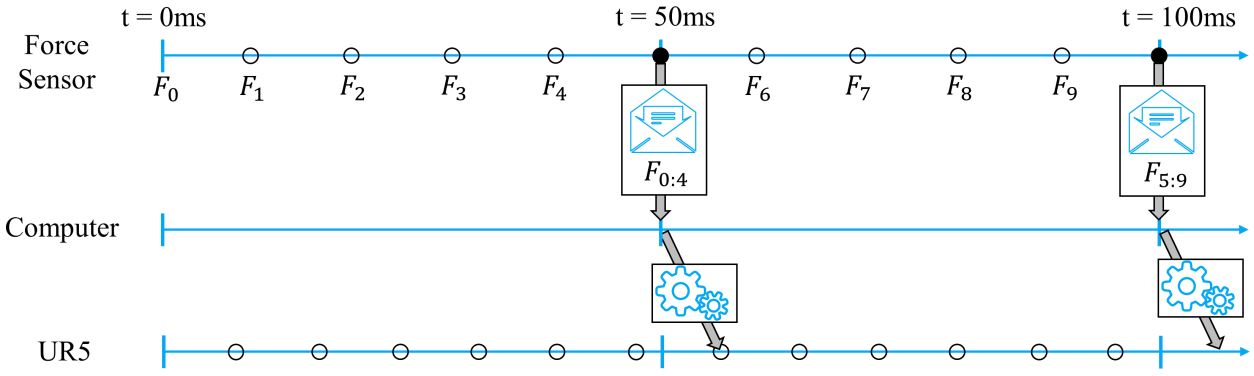

Figure 3.4: A visual display of how limited force/torque packet reception rate prevents commanding the robot at its potential rate. The UR5, running at 125 Hz, is able to be commanded at every circle on its timeline yet is only commanded at 20 Hz due to slow force arrival at the computer.

Kalman filtering is typically known for performing sensor fusion between multiple signals that vary in accuracy and precision to produce an accurate and precise state estimate. It is also typically used for its predictive estimator capabilities when a sensor signal is lost, and is useful in cases such as a GPS passing through a tunnel. The filter state estimate is made based on known covariance of sensor noise, estimated covariance of action

uncertainty, and observation of past states and how they compared with their given estimation at the time. Kalman filters are considered "optimal filters" when assuming cases of Gaussian sensor and action noise that is independent (i.e. noise in f_x is unrelated to noise in f_y and f_z).

An application of Kalman filtering, "Kalman smoothing," does not require the fusion of multiple sensor inputs for state estimation but instead relies on some assumption of the state and its derivatives. For example, we have implemented a "constant acceleration Kalman filter" where the state is the force, first derivative of force (velocity), and second derivative of force (acceleration) concatenated into a single measurement. The result of Kalman smoothing is noise attenuation (low-pass filter) coupled with predictive capabilities that aid sensor interpolation, artificially increasing the data sample rate with some confidence. Kalman smoothing is theoretically advantageous over other low-pass IIR and FIR filters (including Butterworth) for dynamic systems since it uniquely considers *a priori* noisy system observations and covariances, and adapts to enhance closed-loop filtering.

Research on including Kalman filtering in admittance control loops have achieved good results, notably in tremor suppression [34, 35]. We employed Kalman filtering on readings from the Robotiq to (1) smooth force/torque noise through state estimation tuned by observation in real-time, and (2) infer inter-packet force/torque readings to speedup the possible robot command rate. This is illustrated in Fig. 3.5.

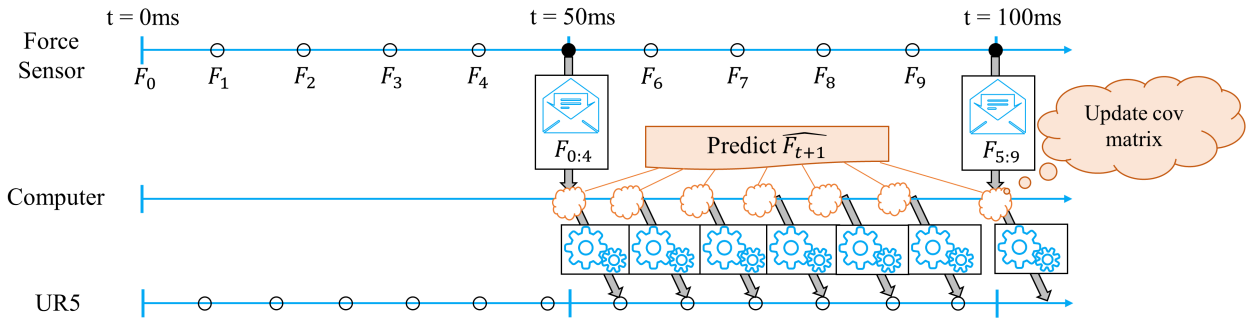

Figure 3.5: A visual display of how Kalman filtering was used to "upsample" low-rate, ground-truth force data so that the robot was commanded as fast as possible. Between force data packets, the Kalman filter predicted future force values allowing for fast and smooth commanding of the UR5 robot thereby enhancing motion transparency.

Our implemented Kalman filter filtering method was invoked at every run-loop of the code, regardless of if a force/torque packet arrived from the Robotiq. If a packet was not received, the filter used its internally stored and tuned covariances to create a state estimate as a means of force/torque interpolation, which was then used to command the robot through admittance control. This was called a "prediction step." If a packet was received, in addition to smoothing the data using the covariance matrices, the filter compared its past predictions to the true measurements reported by the sensor and updated its internal covariances accordingly to improve future predictions. This was called both a "prediction and update step."

The algorithm was built on the assumption of approximately constant acceleration between samples, and takes an input vector $m \in \mathbb{R}^{18\times 1}$ of eighteen values: six for the current force/torque, six for the first derivative of the force/torque, and six for the second derivative of the force/torque. Other notable variables include the manually tuned diagonal matrices $R \in \mathbb{R}^{18\times 18}$ representing sensor confidence covariance and $Q \in \mathbb{R}^{18\times 18}$ representing action uncertainty covariance, measurement selector $H = I_{18\times 18}$, persistent state estimate $x \in \mathbb{R}^{18\times 1}$, and transition matrix A

$$A \in \mathbb{R}^{18\times 18} = \begin{bmatrix} 1 & 0 & 0 & 0 & 0 & 0 & dt & 0 & 0 & 0 & 0 & 0 & \frac{1}{2}dt^2 & 0 & 0 & 0 & 0 & 0 \\ 0 & 1 & 0 & 0 & 0 & 0 & 0 & dt & 0 & 0 & 0 & 0 & 0 & \frac{1}{2}dt^2 & 0 & 0 & 0 & 0 \\ 0 & 0 & 1 & 0 & 0 & 0 & 0 & 0 & dt & 0 & 0 & 0 & 0 & 0 & \frac{1}{2}dt^2 & 0 & 0 & 0 \\ & & & \ddots & & & & & & \ddots & & & & & & & \ddots & \end{bmatrix} \tag{3.8}$$

utilizing $dt = 0.008$ for the desired 125Hz filter update rate. The Kalman algorithm can be summarized as the below steps.

Prediction

$$x[t] = Ax[t-1] \qquad \text{(State Estimate)}$$

$$P = (APA^T) + Q \qquad \text{(Predicted Error Covariance)}$$

Update

$$S = HPH^T + R \qquad \text{(Pre-fit Residual Covariance)}$$

$$K = PH^T S^{-1} \qquad \text{(Optimal Gain)}$$

$$y = m - Hx[t] \qquad \text{(Pre-fit Residual)}$$

$$x[t] = x[t] + Ky \qquad \text{(Updated State Estimate)}$$

$$P = (I - KH)P \qquad \text{(Update Estimate Covariance)}$$

After the above algorithm was implemented, the Q and R covariances were tuned. Matrix R, characterizing sensor noise, was found deterministically as the covariance of the sensor readings while at steady-state. This matrix was calculated by collecting 60 seconds of force sensor data while the robot was at rest, then using the MATLAB `cov` command. Since Kalman filtering is meant for cases of independent noise between states, it was important for the calculated covariance to be approximately a diagonal matrix (which it was). Matrix Q, characterizing user action uncertainty (i.e. noise), traditionally cannot be found deterministically and was therefore tuned to produce the desired filtering response. This matrix was initially tuned to minimize overshoot and phase-lag (which would be felt as "inertia") using a MATLAB Kalman simulator that was written, and then further tuned on the physical robot based on qualitative user feedback.

3.2.4 Admittance Control

3.2.4.1 In-Air Admittance Control

Admittance control, ignoring probe forces, was implemented using linear force-to-velocity gains to convert hand forces and torques measured by the Robotiq force sensor into Cartesian velocities commanded to the robot. The general equation using α for slope and

η for expected noise was:

$$\dot{x} = \begin{cases} 0 & | \vec{F}_{hand} | \leq \eta \\ sgn(\vec{F}_{hand}) \cdot \alpha \left(| \vec{F}_{hand} | - \eta \right) & | \vec{F}_{hand} | > \eta \end{cases} \tag{3.9}$$

This function has a deadband zone when the measured force is within the noise threshold $[-\eta, \eta]$ to attenuate force noise leading to vibration, but otherwise increases linearly with force. A sample plot is shown below.

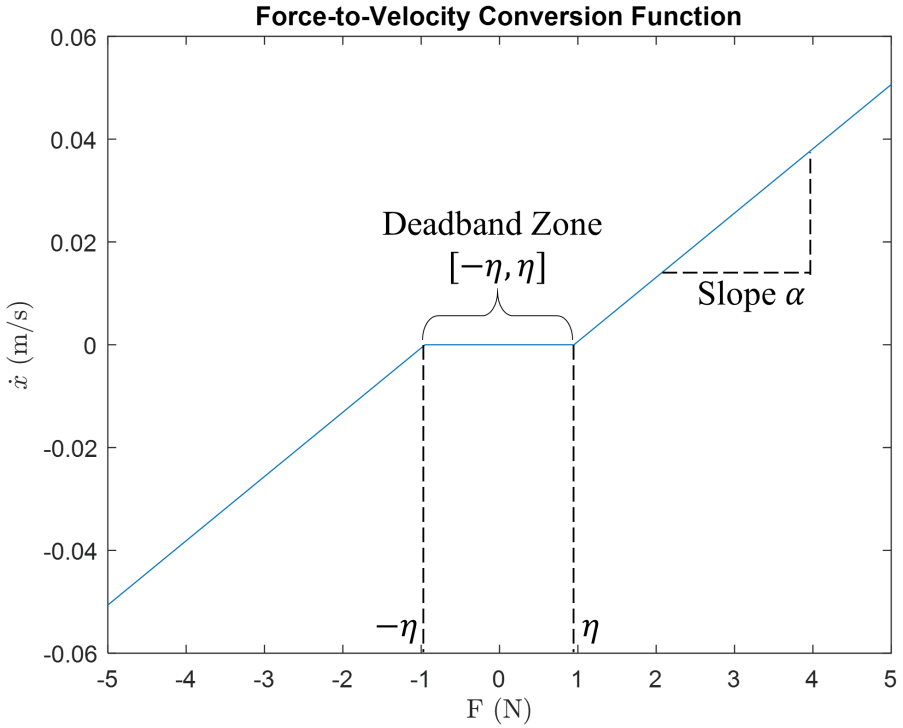

Figure 3.6: A graphical view of the piecewise linear admittance control function to convert forces into commandable velocities. The deadband zone helped attenuate the translation of force noise into vibration at the cost of less responsive behavior, and the slope could be tuned to speed up or down the robot response.

The control constants were tweaked through qualitative feedback to be $\alpha = 0.0125$, $\eta = 0.95$ for the x/y-directions and $\alpha = 0.0125$, $\eta = 0.25$ for the z-direction. The z-direction was given a smaller noise threshold since the Robotiq force sensor has less noise in the z-direction (shown in Section 3.3.2), and it makes the system more responsive for z-direction palpation during scanning.

The use of linear admittance control gains was believed to be an upgrade from the sigmoidal gains used in [26]. After evaluating the plots of motion for both admittance control schemes provided in Section 3.3.3 and testing with the robot setup, it was determined that the sigmoidal gains likely introduced nonlinearities into the Kalman filter, which is a linear quadratic estimator and not designed to model nonlinear behavior. While the proposed admittance control function is only piecewise linear and non-differentiable, it still resulted in more transparent control than the sigmoidal function. It should be noted that since [26] used frequency-domain filtering instead of Kalman filtering, their work may not have been as affected by the nonlinearities of the sigmoidal curve.

3.2.4.2 Compensating for Probe Contact Forces

A second force sensor, as stated before, would be necessary for discerning probe forces from hand forces when a scan is occurring. Without discerning, the "equal-and-opposite" forces exerted by the elastic phantom/patient onto the probe upon contact will be detected as part of $\vec{F}_{hand}$ by the Robotiq sensor and cause the robot to "bounce" off the scanning surface since the force is in the opposite direction. Therefore, what has been referred to as $\vec{F}_{hand}$ all along is actually $\vec{F}_{hand} = \widetilde{\vec{F}}_{hand} + \vec{F}_{probe}$, where $\widetilde{\vec{F}}_{hand}$ is the true force/torque exerted by the user's hand. In the in-air case, $\vec{F}_{probe} = 0$ meaning $\vec{F}_{hand} \equiv \widetilde{\vec{F}}_{hand}$ which is why we could use equation (3.9) for admittance control previously. When scanning, however, $\vec{F}_{probe}$ is nonzero due to contact with the patient and therefore the admittance control becomes

$$\dot{x} = \begin{cases} 0 & \mid \widetilde{F}_{hand} \mid \leq \eta \\ sgn(\widetilde{F}_{hand}) \cdot \alpha \left(\mid \widetilde{F}_{hand} \mid - \eta \right) & \mid \widetilde{F}_{hand} \mid > \eta \end{cases} \tag{3.10}$$

or equivalently

$$\dot{x} = \begin{cases} 0 & | \vec{F}_{hand} - \vec{F}_{probe} | \leq \eta \\ sgn(\vec{F}_{hand} - \vec{F}_{probe}) \cdot \alpha \left(| \vec{F}_{hand} - \vec{F}_{probe} | - \eta \right) & | \vec{F}_{hand} - \vec{F}_{probe} | > \eta \end{cases} \tag{3.11}$$

Unfortunately, due to hardware issues with our second force sensor embedded in the probe housing that were described in Section 3.1.1, we were unable to fully test this algorithm. However, the method we describe above is sound and is appropriate to include for potential future directions.

3.3 Results

3.3.1 Gravity Compensation

The gravity compensation procedure described in Section 3.2.2 was performed and resulted in $-mg = -4.7631\ N$, and $\vec{p}_{COM,xy} = (-0.01250\ m, -0.00033\ m)$. These results make sense since the probe (including housing) weighed about 0.48 kg as measured on a scale, and had a second force sensor embedded in the housing about a centimeter offcenter in the negative x-direction and a negligible offset in the y-direction.

These parameters were tested on 32 static robot poses with the ideal result being that 0 N of force and 0 N·m of torque are expressed after compensation regardless of the uncompensated reading. The results of the compensation are shown below, with green arrows showing significant improvement from compensation and red arrows showing significant worsening from compensation.

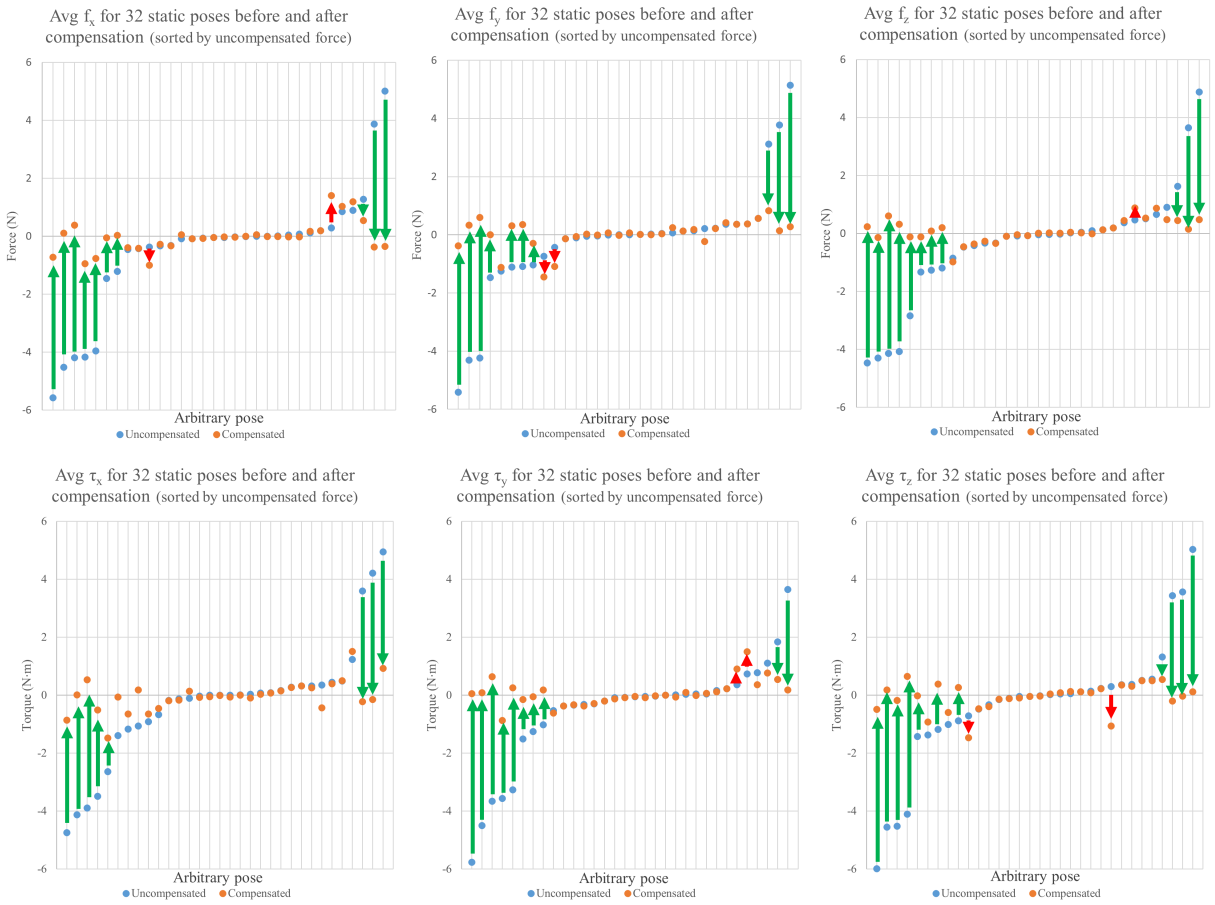

Figure 3.7: A graphical view of the gravity compensation results. Ideal compensation would result in the blue dots converging to orange dots along the x-axis meaning that no matter the probe orientation, the algorithm could always predict the weight contribution of the tool to the force sensor.

As seen, the compensation improves most all of the force readings by bringing them toward zero. The average absolute force for all poses after compensation decreased from 1.21 N to 0.32 N, and the average absolute torque after compensation decreased from 1.25 N·m to 0.33 N·m. Since almost all of the poses experienced an improvement through compensation and most poses experienced a compensation to within the observed noise range of the sensor, the compensation was deemed successful.

Using data from the same 32 static poses, radar plots were constructed to show which robot orientation caused the most error after compensation.

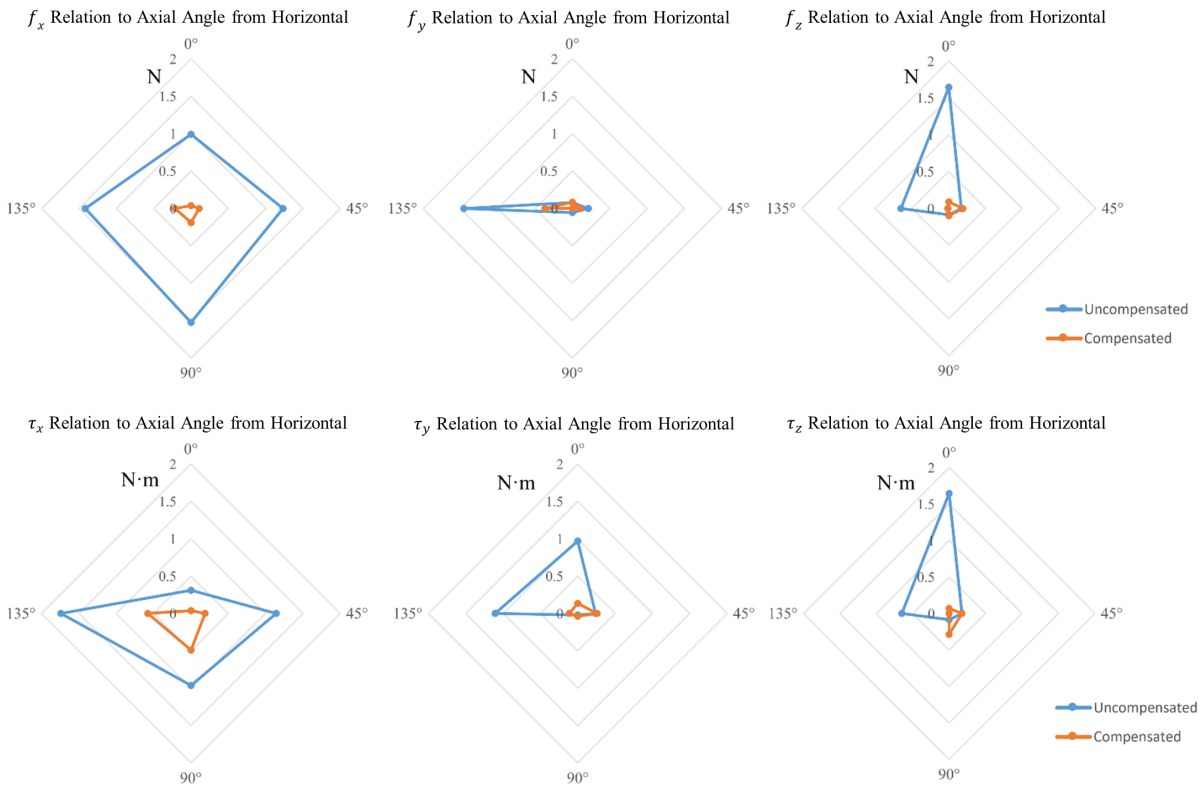

Figure 3.8: A radar view of the gravity compensation results to show compensation effectiveness for multiple angles. Ideally, these plots would have a uniformly shaped polygon close to the zero force point meaning that compensation was approximately the same for all angles.

These radar plots are somewhat inconclusive, but there appears to be a possible relation between compensation accuracy and pose orientation in some cases. For example, compensation of f_x was quite uniform despite the angle of the probe with respect to horizontal. However, compensation of f_y was very accurate except for $135°$ from horizontal. This is interesting since one would expect the accuracy for $135°$ and $45°$ from the horizontal to have the same accuracy. However, it is likely that cable drag plays a role here since the cable protrudes from the housing along the y-axis and was not routed in a way that kept it in a deterministic position. Therefore, the tool weight was felt differently when the y-axis was $135°$ and $45°$ from the horizontal. Similar comments can be made about the other forces and torques as well. Future work should further consider eliminating cable drag, or making it more deterministic, through a mechanical mechanism.

3.3.2 Kalman Filtering

Kalman filtering was implemented as described in Section 3.2.3. Force and torque data were collected with the robot in multiple static poses to show noise attenuation, as well as with the robot manipulated around the workspace to show potential phase-lag and overshoot.

The time-domain results of Kalman filtering on $\vec{F}_{hand}$ noise while the robot was in a static pose are summarized in Table 3.1 and graphed in Fig. 3.9. The filter significantly reduced force noise in the x-, y-, and z-directions respectively: the standard deviation decreased by an average 38% and the maximum absolute noise decreased by an average 40%. It should be noted that the sensor force noise was inherently lower in the z-direction, a factor that led our team to use a different set of admittance control gains and Kalman covariances (with stronger trust in the measured sensor reading) for forces in the z-direction versus those in the x- and y-directions. The filter significantly reduced torque noise about the x-, y-, and z-axes respectively: the standard deviation decreased by an average 26% and the maximum absolute noise decreased by an average 36%. It should be noted that the sensor torque noise was inherently higher about the z-axis, which led our team to use a different set of admittance control gains and Kalman covariances (with less trust in the measured sensor reading) for torques about the z-axis versus those about the x- and y-axes.

Table 3.1: Standard deviation and maximum absolute value of $\vec{F}_{hand}$ noise, before and after Kalman filtering. Filtering reduces both metrics significantly.

	Standard Deviation		Maximum Absolute Value	
	Unfiltered	Kalman Filtered	Unfiltered	Kalman Filtered
f_x	0.31 N	0.19 N	1.05 N	0.65 N
f_y	0.31 N	0.20 N	0.75 N	0.45 N
f_z	0.13 N	0.08 N	0.28 N	0.16 N
τ_x	0.007 N·m	0.006 N·m	0.017 N·m	0.011 N·m
τ_y	0.008 N·m	0.006 N·m	0.022 N·m	0.015 N·m
τ_z	0.015 N·m	0.009 N·m	0.046 N·m	0.027 N·m

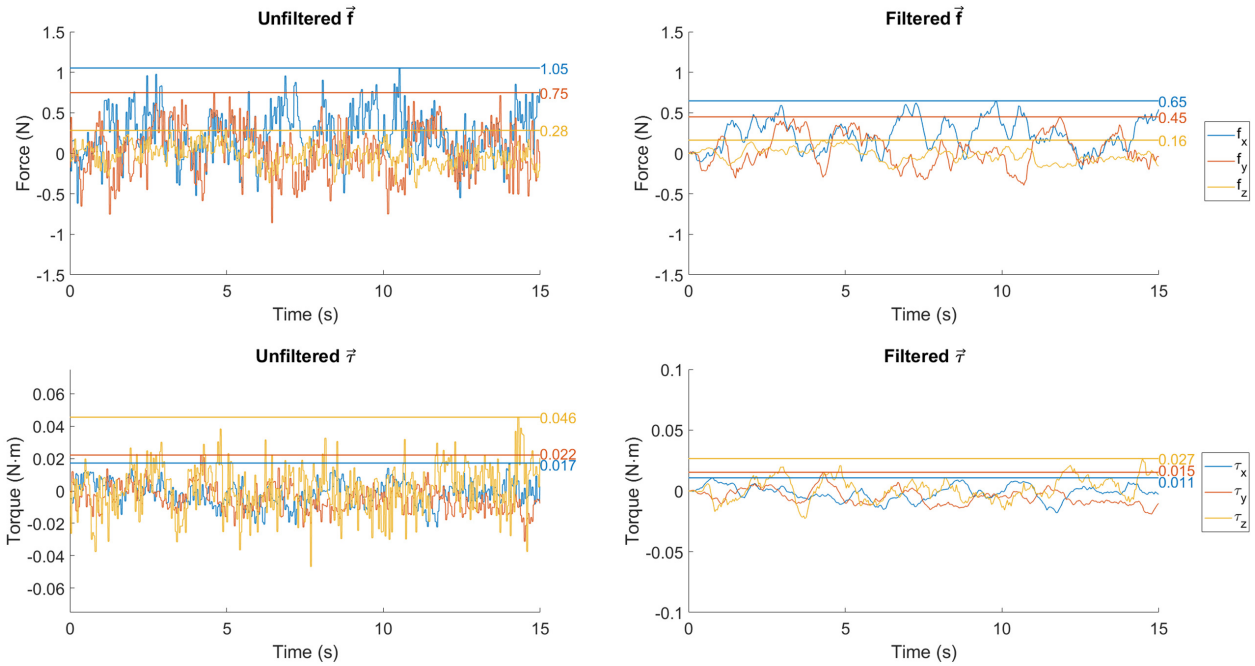

Figure 3.9: The time-domain effects of the tuned Kalman filtering on $\vec{F}_{hand}$ noise measured while the robot was in a stationary pose. Kalman filtering significantly smooths the noise, decreasing its maximum force amplitude by 40% and maximum torque amplitude by 36%.

The timeseries data above was brought into the frequency domain for analysis. Power spectrum plots are provided in Fig. 3.10. The filter increased the rate of frequency dropoff, attenuating frequencies greater than 1 Hz by about -30 dB/decade compared to the unfiltered which attenuates about -20 dB/decade. The increased dropoff of high frequencies highlights the low-pass filter characteristics of Kalman filtering. This behavior is desired to smooth perceived hand guidance and attenuate hand tremor, since intentional hand forces are typically low frequency ($\leq$ 4 Hz) [36].

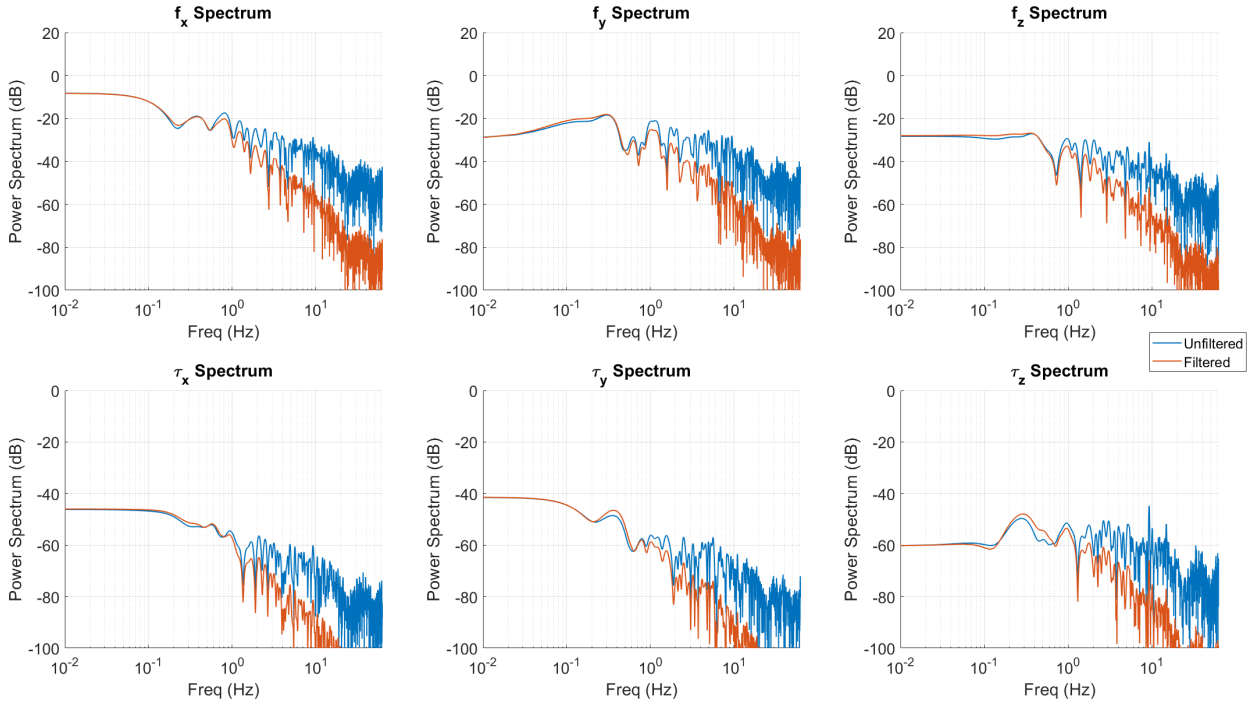

Figure 3.10: The frequency-domain effects of the tuned Kalman filtering on $\vec{F}_{hand}$ noise measured while the robot was in a stationary pose, shown as a power spectrum. Kalman filtering has a steeper dropoff, resulting in more attenuation of high frequencies.

A Butterworth filter was ideated at the start of this research as a potential frequency-domain filtering strategy. Therefore, the same Kalman filtered data was also compared to a 5th-order Butterworth filter with a cutoff frequency of 5 Hz implemented in simulation. The results of filtering the force/torque signals with both the Kalman and Butterworth filters are shown in Fig. 3.11. It can be seen that the Kalman and Butterworth filters smooth the noise similarly, however the Butterworth filter incurs significant phase-lag compared to the Kalman filter.

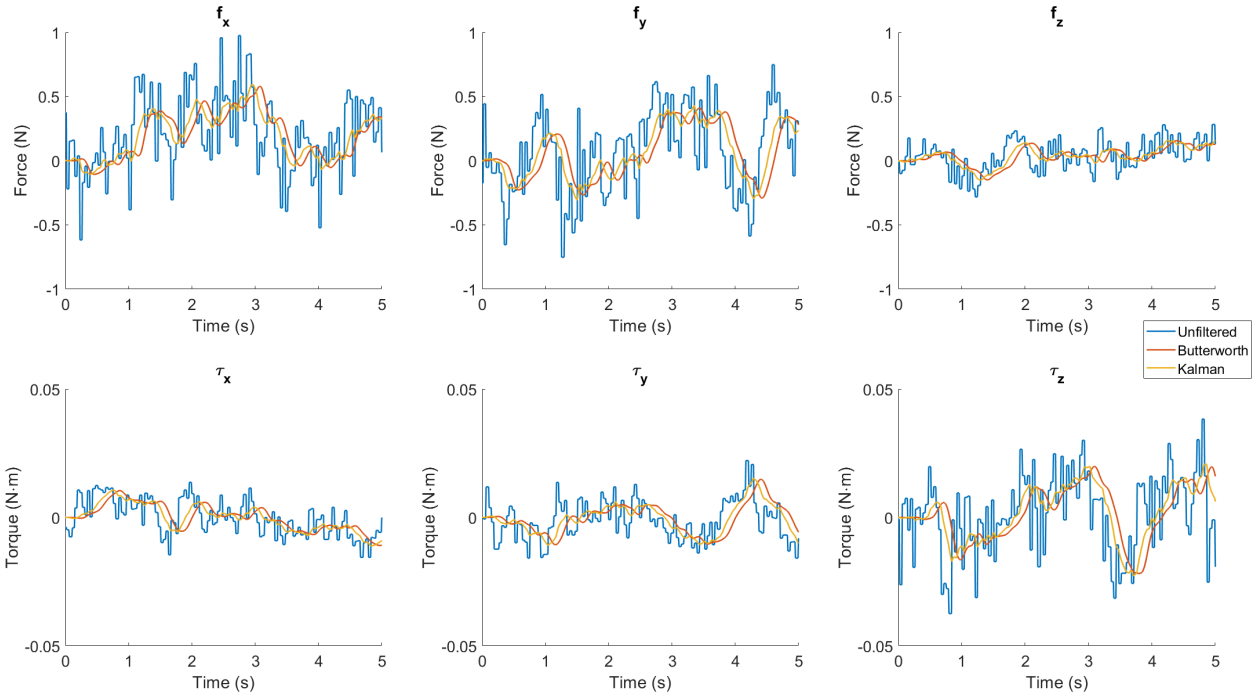

Figure 3.11: The result of the tuned Kalman filter on $\vec{F}_{hand}$ noise while the robot was stationary compared to a 5$^{\text{th}}$-order Butterworth filter with a 5 Hz cutoff frequency (evaluated in simulation). Butterworth filtering incurs significant phase-lag compared to Kalman filtering.

The plots in Figs. 3.9 and 3.10 show that the Kalman filter was successful in attenuating noise for the force/torque sensor while the robot was in a static pose. The worst-case noise was approximately cut by over one-third in each direction, and the standard deviation decreased by over one-quarter. This is useful since the deadband zone of the admittance control algorithm (3.9) can be made narrower when η is smaller versus when using unfiltered data, which makes the motion feel "snappier" and more "transparent" to the user. Additionally, the Kalman filtering appeared to be superior to frequency-domain filtering using a Butterworth filter as it had less phase-lag and similar noise amplitude. Future work could try to couple a Butterworth and Kalman filter in series, but this is not guaranteed to produce a better result.

Force data was also collected while manipulating the robot in small circles around the workspace to measure phase-lag and accuracy. The results of this analysis are shown in Fig. 3.12. From the plots, it could be graphically determined that there was approximately

8 ms of phase-lag added by the filter and an almost negligible amount of undershoot and overshoot. The rectangular shape of the unfiltered force readings can be attributed to the fact that a force packet only arrived every 50 ms, and the force value is held until the next packet arrives. The Kalman filter is much smoother since a new value is predicted every 8 ms (i.e. 125 Hz). This prediction rate also explains the observed phase-lag in the plot – it takes one 8 ms filter cycle to produce a new velocity in response to a change in hand force.

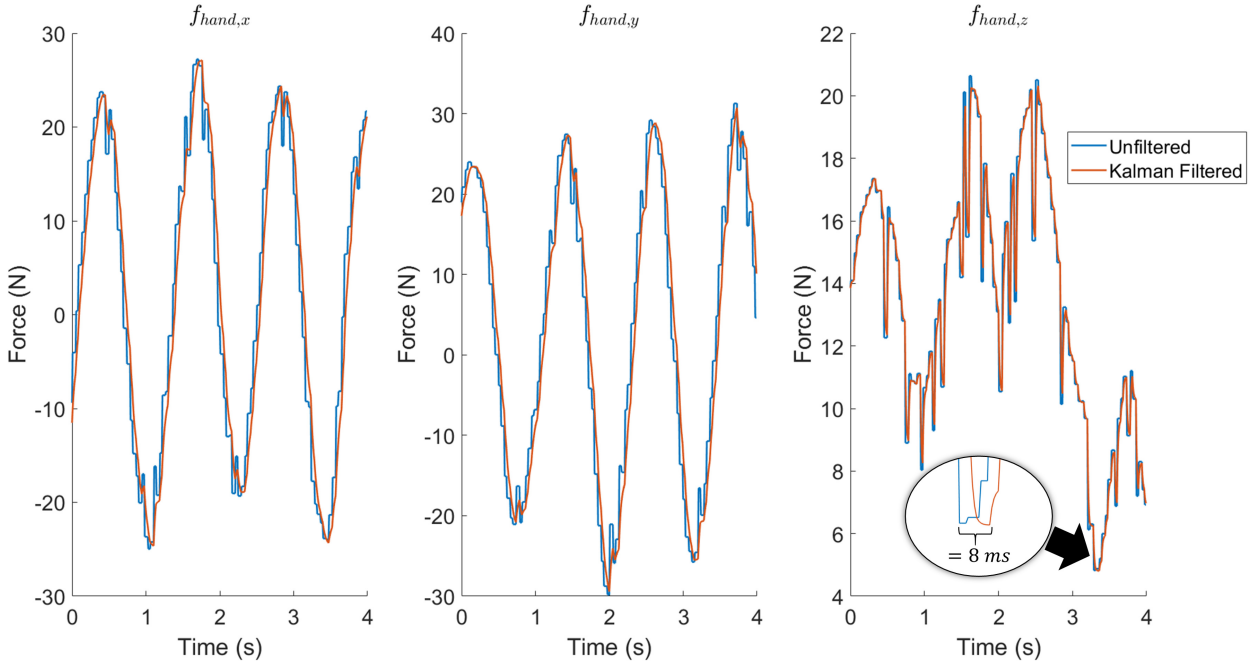

Figure 3.12: The result of the tuned Kalman filter on $\vec{F}_{hand}$ while maneuvering the robot around the workspace. The filter introduces approximately 8 ms of phase-lag (about equal to the 125 Hz update rate of the filter) and has very small amounts of overshoot and undershoot.

The measured phase-lag of about 8 ms seems small and did not interfere with the user experience of moving the robot by hand. However, users did notice “inertia” once they stopped applying hand forces to the robot. This could be attributed to the fact that “human-in-the-loop” helps compensate for phase-lag and overshoot while a user is operating the robot, but once the user stops applying forces the lag and inaccuracies become much more noticeable.

3.3.3 In-Air Admittance Control

Admittance control was implemented as described in Section 3.2.4. A plot showing the commanded velocity difference when using the linear gains proposed in this work versus the sigmoidal gains used in [26] is shown below in Fig. 3.13.

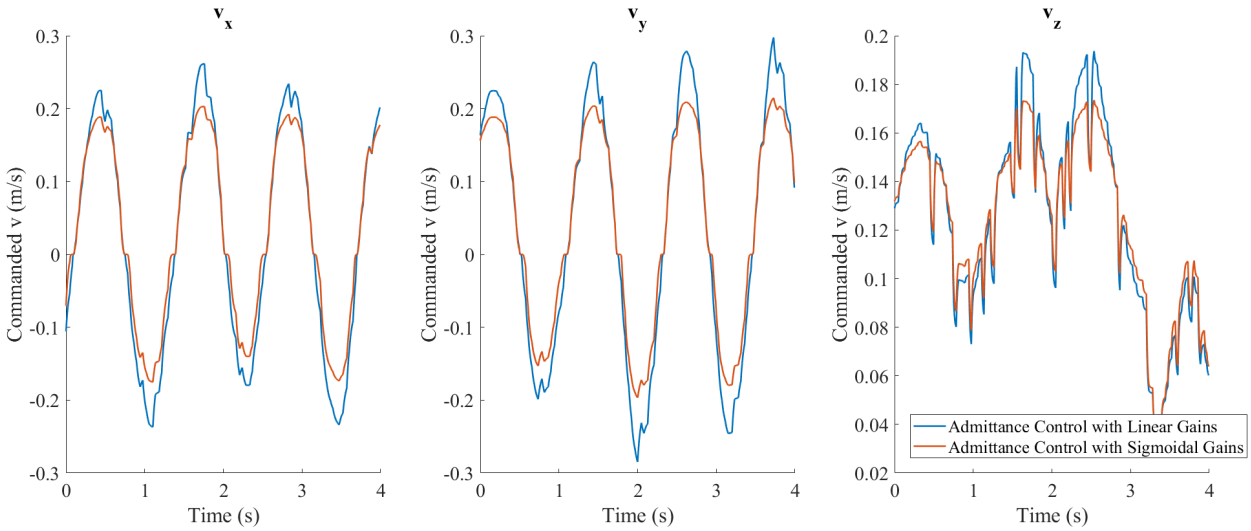

Figure 3.13: The result of the piecewise linear admittance control algorithm proposed in this work versus the sigmoidal algorithm proposed in [26]. The sigmoidal function undershoots the linear one, and also introduces nonlinear behavior at the 0 m/s crossing.

While both curves appear to be smooth, the sigmoidal force-to-velocity conversion clearly undershoots the linear force-to-velocity conversion result. Additionally, the sigmoidal gains cause a nonlinear behavior as the velocity crosses 0 m/s which is where the conversion function enters a deadband zone. We hypothesized that this nonlinear behavior is difficult for the developed Kalman filter to characterize in its state estimates making linear gains advantageous for smaller forces near the deadband zone.

3.4 Planned Validation HIRB Study

The previous section sought to verify that the developed filtering strategy and admittance control loop performed well quantitatively. However, the ultimate validation of our solution

against the original clinical problem of ultrasonographer ergonomics would require a user study that measures sonographer muscle exertion during scanning both with and without collaborative robot assistance. An HIRB study was proposed and approved, but could not be performed in time for this work due to the COVID-19 disruptions. We briefly outline the protocol below, as it may be useful to future researchers.

The study involved outfitting consenting participants with disposable surface electromyography (sEMG) electrodes on their dominant forearm and suprascapular fossa for measuring muscle exertion during scans, as suggested by [37]. A previous study on quantifying the change of ultrasonographer exertion during robot-assisted US used force sensors on the probe grip, however is it difficult to correlate hand "squeezing" force to forearm and shoulder strain and microtrauma that causes ultrasonographer harm. Then, the participant would be instructed to perform two tasks: (1) hold a probe still against a phantom for a minute, and (2) scan a custom phantom, tracing a convoluted, hyperechoic fiducial tube embedded within while applying a constant 20 N of force (approximately 4.4 lbs). Each tasks would be performed four ways: (1) freehand, (2) freehand with visual force feedback, (3) robot-assisted without force constraint, and (4) robot-assisted with a maximum force constraint. This results in a total of eight experiments per participant, where multiple trials of each experiment could be performed for more reliable results. Additionally, at the end of the experiment, participants would be issued a standard NASA Task Load Index (TLX) survey about their perceived operator workload and strain.

Experiment (1) would be analyzed in terms of probe contact force stability, and participant muscle exertion as measured by the sEMG system. US images collected during the experiment could also be analyzed for movement via speckle decorrelation. Experiment (2) would be analyzed in terms of probe contact force stability, participant muscle exertion, and tracking error of the convoluted tube via computer vision applied to cine US images. Aside from these experiments, the TLX survey would also be analzyed to gain insight as to the robotic system's utility and intuitiveness. An anticipated result would

show that scanning with robot assistance and a maximum force constraint leads to more stable probe contact force, more stable cine US acquisition, less ultrasonographer muscle exertion, and less operator task load.

3.5 Discussion and Conclusion

The results of this work are significant on two fronts related to the earlier proposed goals. First, the smooth admittance control scheme based around Kalman filtering appears to be promising for reducing muscle strain while scanning and augmenting sonographer scanning ability. While a full user study with sEMG sensing would be needed for complete validation, the preliminary results and qualitative feedback certainly make it appear that the proposed solution would be helpful on these fronts. Second, the functional C++ filter implementation is important for any future work involving robotics and US at JHU. Since the code was built on the CISST/SAW libraries, this work is very extensible and the general hand-over-hand control framework could be applied to numerous (including non-US) applications that could benefit from improved control.

The most important future development should be outfitting the probe holder with a second, functional force sensor for differentiating probe contact forces from hand forces. Significant thought should be put into a new mechanical design of a probe holder that distributes probe forces into the force sensor without spatially displacing the probe. Once this is done, a complete, HIRB-approved user study should be conducted to validate that our system is meeting end-user needs and providing a physical health benefit to them. It is our ultimate hope that our system alleviates ultrasonographer musculoskeletal strain and improves their quality of life. It is also important not to forget another motivator of improved force filtering and hand-over-hand control – the work performed here should be ported to the previously described dual-robotic USCT system to enable physicians to control the probes smoothly by hand.

Chapter 4

Conclusions

4.1 Summary

In the first half of this work, we introduced a dual-robotic system for performing USCT imaging of the in vivo prostate. Our work was motivated by prior research that showed comparable diagnostic utility for detecting prostate pathology between USCT and MRI. Since commercial scanners traditionally use a water-tank approach that is impractical for imaging deep in vivo anatomy, we pursued and implemented a novel dual-robotic approach utilizing robots outfitted with an off-the-shelf TRUS and abdominal probe respectively for capturing USCT slices of the prostate in an unsubmerged environment. We chose the TRUS probe to be the joystick controlled, physician guided element of the system, opting for the abdominal probe to autonomously servo on the pelvic region to maintain alignment with the TRUS probe line-of-sight for the transmission US imaging necessary for USCT reconstruction. With the two robots rigidly affixed to each other in a custom 80/20 T-Slot rig, three calibrations (two BXp, one A=XB) were performed such that all coordinate transforms in the scene were calculable at any time. All calibrations had submillimeter accuracy leading us to believe the repeatability of the overall system, also considering the respective accuracies of the robotic arms, is sufficient for tomog-

raphy based on prior standards. A significant motion control framework was proposed and implemented for autonomous abdominal probe manipulation, which was conceptually similar to hybrid force-position control. The framework aimed to keep the abdominal probe aligned with the TRUS probe as the TRUS was rotated intraluminally, while also performing impedance-controlled gentle convex contour tracking of the pubic region to maintain contact with the applied coupling gel. The motion control framework was tested on a pelvic phantom: we rotated the TRUS probe and observed the abdominal probe traverse across the phantom's pubic region. The framework produced satisfactory practical results, and graphing the Cartesian positions of both probes during the traversal with respect to a static frame showed the TRUS rotating in-place (at least within a few mm due to calibration inaccuracy) and the abdominal probe always oriented toward the TRUS, following a convex pathway resembling the convex pubic region. Further imaging verification was done on the phantom to (1) prove that a sufficient acoustic window existed for transmission US of the prostate that avoided the pubic bone and bladder, (2) investigate the depth at which the phantom will cause acoustic signal attenuation, and (3) quantify how many slices of the phantom prostate we could acquire, which is a limiting factor in USCT reconstruction resolution. The developed system has important implications for USCT scanning of the prostate and, among other developments, we look toward future progress in collecting transmission US slices with the system to test tomographic reconstructability.

In the second half of this work, we proposed and implemented an improved force/torque filtering mechanism based on Kalman filtering. Initially motivated to provide the USCT system with the option of hand guidance and smooth the impedance control used for convex contour tracking, we broadened our clinical application to improving ultrasonographer ergonomics with a hand guidable US "power-steering" robot. Previous research in this field had lacked motion transparency, likely due to suboptimal force filtering, a slow force reading rate, sigmoidal admittance gains, and its MATLAB implementation. We proposed the use of Kalman filtering for performing force smoothing and inferring inter-packet

force/torque readings as a means to artificially upsample the data with some confidence. We pursued this method since human hand movements during ultrasonography are relatively low frequency and linear, and Kalman filtering adaptively characterizes plant state and predicts future trajectories, effectively acting as a low-pass filter. We also chose to use linear admittance control gains with a noise deadband zone, which was more appropriate than nonlinear sigmoidal gains that could cause an issue with the linear state estimation of the Kalman filter. The results of the hand-over-hand system were overall satisfactory, and seemed to be a large improvement over past research on the topic. The Kalman filter reduced at-rest average noise by over one-quarter, and reduced at-rest maximum absolute noise by over one-third. It also significantly smoothed commanded robot velocities with an observed phase-lag of only 8 ms. Additionally, our gravity compensation procedure successfully reduced the measured weight contribution of the US probe to within the noise range of the sensor. The developed system has important implications for reducing the occupational hazards of ultrasonographers, but also has the ability to improve any hand-guided robot procedure.

4.2 Future Work

The discussion of future work has been distributed throughout this thesis, and we will briefly summarize some key ideas here.

Before any future work on the USCT system, further validation and verification should be performed. Key physician stakeholders should be identified and encouraged to use the system as a means of validation and garnering feedback for future development. From this feedback, more clearly defined requirements should be set for the system to guide verification. With appropriate requirements identified, in-plane and out-of-plane accuracies should be individually identified through water-tank testing. This test would involve statically submerging the TRUS probe in a water-tank while traversing the abdominal probe

across the water surface, above the TRUS transducer face, in a grid pattern with various rotations. The resulting channel data would provide valuable insight into the alignment of the two probes. The system should also be tested on phantoms representing a larger body habitus to confirm the effectiveness of the robot contour tracking motion framework and verify that US energy can penetrate large depths without being too attenuated and scattered for reconstruction. Only after extensive testing should more features be considered. For instance, one feature could be a novel, gradient descent guided dual-robot calibration algorithm that autonomously aligns the two probes in a way that maximizes and centralizes the channel data received by the Rx probe. Another interesting development would be making the TRUS probe hand guidable using the collaborative control framework we proposed, instead of joystick controlled. Alternatively, the hand guided probe can be set to the abdominal probe instead of the TRUS. Other feedback has suggested adding admittance control to the joystick controlled TRUS probe as a safety mechanism, in case the patient is shifted mid-procedure. Additionally, the TRUS-holding robot can be replaced with a 2-DoF linear/rotational stage if deemed more clinically practical.

The main future work on the collaborative, hand-over-hand robot platform should involve a complete user study that quantitatively measures the change in ultrasonographer exertion through sEMG (or similar sensing) and task load surveys. The study should also investigate the effect of robot assistance on US image stability, whether the probe is held statically or tracing an embedded fiducial. After testing, future developments can be considered. One pain point of Kalman filtering is tuning the covariance matrices R and Q. While sensor covariance R can be approximated from sensor noise, user action uncertainty Q must be manually tuned and is therefore likely to be suboptimal. An automated tuning approach would be beneficial, as would an extended or unscented Kalman filter that includes nonlinear considerations.

4.3 Final Word

The realm of robot-assisted US procedures is exciting and dynamic. Combining the real-time, non-ionizing, and cheap US imaging modality with robot guidance can unlock novel imaging paradigms that have clinical utility similar to CT and MRI scanning and interventional guidance. USCT is a promising thrust in this direction. Our proposed dual-robotic approach makes it feasible for prostate imaging. Likewise, our proposed hand-over-hand control framework enabled by force/torque smoothing and inference through Kalman filtering has shown superior results over past implementations and has important implications for improving ultrasonographer musculoskeletal strain. There is an extensive amount of future work on both of these platforms, and further strides toward clinical trials, user studies, and overall practical usage should be pursued. Ultimately, our novel advancements in robot-assisted US, between USCT and collaborative control, is the starting point for affordable, convenient, and accurate diagnostic studies and interventional procedures.

Bibliography

[1] Vincent Chan and Anahi Perlas. Basics of ultrasound imaging. In *Atlas of ultrasound-guided procedures in interventional pain management*, pages 13–19. Springer, 2011.

[2] José Seabra and Joao Miguel Sanches. Rf ultrasound estimation from b-mode images. In *Ultrasound Imaging*, pages 3–24. Springer, 2012.

[3] Bruce R Douglas, J William Charboneau, and Carl C Reading. Ultrasound-guided intervention: expanding horizons. *Radiologic Clinics of North America*, 39(3):415–428, 2001.

[4] Leonard Marks, Shelena Young, and Shyam Natarajan. Mri–ultrasound fusion for guidance of targeted prostate biopsy. *Current opinion in urology*, 23(1):43, 2013.

[5] Barys Ihnatsenka and André Pierre Boezaart. Ultrasound: Basic understanding and learning the language. *International journal of shoulder surgery*, 4(3):55, 2010.

[6] Ki Jinn Chin, Anahi Perlas, Vincent WS Chan, and Richard Brull. Needle visualization in ultrasound-guided regional anesthesia: challenges and solutions. *Regional Anesthesia & Pain Medicine*, 33(6):532–544, 2008.

[7] Bilal Malik, Robin Terry, James Wiskin, and Mark Lenox. Quantitative transmission ultrasound tomography: Imaging and performance characteristics. *Medical Physics*, 45(7):3063–3075, 2018.

[8] Alexis Cheng, Yuttana Itsarachaiyot, Younsu Kim, Haichong K Zhang, Russell H Taylor, and Emad M Boctor. Catheter tracking in an interventional photoacoustic surgical system. In *Medical Imaging 2017: Image-Guided Procedures, Robotic Interventions, and Modeling*, volume 10135, page 1013527. International Society for Optics and Photonics, 2017.

[9] Bharat Mathur, Anirudh Topiwala, Saul Schaffer, Michael Kam, Hamed Saeidi, Thorsten Fleiter, and Axel Krieger. A semi-autonomous robotic system for remote trauma assessment. In *2019 IEEE 19th International Conference on Bioinformatics and Bioengineering (BIBE)*, pages 649–656. IEEE, 2019.

[10] Bo Meng, Ying-ying Zhao, Lei Chen, Fereshteh Aalamifar, Xue-jun Liu, and Emad Boctor. Robot-assisted mirror ultrasound scanning for deep venous thrombosis detection using rgb-d sensor. *Multimedia Tools and Applications*, 75(22):14247–14261, 2016.

[11] Tian Xie, Mahya Shahbazi, Yixuan Wu, Russell H Taylor, and Emad M Boctor. Stabilized ultrasound imaging of a moving object using 2d b-mode images and convolutional neural network. In *Medical Imaging 2020: Image-Guided Procedures, Robotic Interventions, and Modeling*, volume 11315, page 113150C. International Society for Optics and Photonics, 2020.

[12] Haichong K Zhang, Rodolfo Finocchi, Kalyna Apkarian, and Emad M Boctor. Co-robotic synthetic tracked aperture ultrasound imaging with cross-correlation based dynamic error compensation and virtual fixture control. In *2016 IEEE International Ultrasonics Symposium (IUS)*, pages 1–4. IEEE, 2016.

[13] CISST libraries and Surgical Assistant Workstation (SAW). Available: `https://github.com/jhu-cisst/cisst/wiki`.

[14] Freddie Bray, Jacques Ferlay, Isabelle Soerjomataram, Rebecca L Siegel, Lindsey A Torre, and Ahmedin Jemal. Global cancer statistics 2018: Globocan estimates of incidence and mortality worldwide for 36 cancers in 185 countries. *CA: a cancer journal for clinicians*, 68(6):394–424, 2018.

[15] Christopher JD Wallis, Masoom A Haider, and Robert K Nam. Role of mpmri of the prostate in screening for prostate cancer. *Translational andrology and urology*, 6(3):464, 2017.

[16] CJ Harvey, J Pilcher, J Richenberg, U Patel, and F Frauscher. Applications of transrectal ultrasound in prostate cancer. *The British journal of radiology*, 85(special_issue_1):S3–S17, 2012.

[17] Hideki Tanoue, Yoshihiro Hagiwara, Kazuto Kobayashi, and Yoshifumi Saijo. Ultrasonic tissue characterization of prostate biopsy tissues by ultrasound speed microscope. In *2011 Annual International Conference of the IEEE Engineering in Medicine and Biology Society*, pages 8499–8502. IEEE, 2011.

[18] Reza Seifabadi, Alexis Cheng, Bilal Malik, Shun Kishimoto, James Wiskin, Jeeva Munasinghe, Ayele H Negussie, Ivane Bakhutashvili, Murali C Krishna, Peter Choyke, et al. Correlation of ultrasound tomography to mri and pathology for the detection of prostate cancer. In *Medical Imaging 2019: Ultrasonic Imaging and Tomography*, volume 10955, page 109550C. International Society for Optics and Photonics, 2019.

[19] Delphinus Medical Technologies. Softvue system. `http://www.delphinusmt.com/technology/`, 2020. [Online; accessed 11-March-2020].

[20] QT Ultrasound. Quantitative transmission ultrasound: An evolution in breast imaging. `https://www.qtultrasound.com/about-us/`, 2020. [Online; accessed 11-March-2020].

[21] James Wiskin, Bilal Malik, Rajni Natesan, David Borup, Nasser Pirshafiey, Mark Lenox, and John Klock. Full wave 3d inverse scattering transmission ultrasound tomography: Breast and whole body imaging. In *2019 IEEE International Ultrasonics Symposium (IUS)*, pages 951–958. IEEE, 2019.

[22] Rajni Natesan, James Wiskin, Sanghyeb Lee, and Bilal H Malik. Quantitative assessment of breast density: transmission ultrasound is comparable to mammography with tomosynthesis. *Cancer Prevention Research*, 12(12):871–876, 2019.

[23] James W Wiskin, Bilal Malik, Rajni Natesan, Nasser Pirshafiey, John Klock, and Mark Lenox. 3d full inverse scattering ultrasound tomography of the human knee (conference presentation). In *Medical Imaging 2019: Ultrasonic Imaging and Tomography*, volume 10955, page 109550K. International Society for Optics and Photonics, 2019.

[24] Mark Lenox, John Klock, Cathy Ruoff, Nasser Pirshaifey, Robin Terry, Bilal Malik, and James Wiskin. 3d inverse scattering in wholebody ultrasound applications (conference presentation). In *Medical Imaging 2019: Ultrasonic Imaging and Tomography*, volume 10955, page 1095511. International Society for Optics and Photonics, 2019.

[25] Fereshteh Aalamifar et al. *Co-robotic Ultrasound Tomography: A New Paradigm for Quantitative Ultrasound Imaging*. PhD thesis, Johns Hopkins University, 2016.

[26] Rodolfo G Finocchi et al. Co-robotic ultrasound imaging: A cooperative force control approach. Master's thesis, Johns Hopkins University, 2016.

[27] Ting-Yun Fang, Haichong K Zhang, Rodolfo Finocchi, Russell H Taylor, and Emad M Boctor. Force-assisted ultrasound imaging system through dual force sensing and admittance robot control. *International journal of computer assisted radiology and surgery*, 12(6):983–991, 2017.

[28] Martin Ackerman, Alexis Cheng, Emad Boctor, and Gregory Chirikjian. Online ultrasound sensor calibration using gradient descent on the euclidean group. pages 4900–4905, 05 2014.

[29] Berthold Horn, Hugh Hilden, and Shahriar Negahdaripour. Closed-form solution of absolute orientation using orthonormal matrices. *Journal of the Optical Society of America A*, 5:1127–1135, 07 1988.

[30] R Lozano and B Brogliato. Adaptive hybrid force-position control for redundant manipulators. In *29th IEEE Conference on Decision and Control*, pages 1949–1950. IEEE, 1990.

[31] Alex Schoenfeld, Jeremy Goverman, Debra M Weiss, and Israel Meizner. Transducer user syndrome: an occupational hazard of the ultrasonographer. *European journal of Ultrasound*, 10(1):41–45, 1999.

[32] Thierry Rousseau, Nicolas Mottet, Guillaume Mace, Carole Franceschini, and Paul Sagot. Practice guidelines for prevention of musculoskeletal disorders in obstetric sonography. *Journal of Ultrasound in Medicine*, 32(1):157–164, 2013.

[33] Fotios Dimeas and Nikos Aspragathos. Learning optimal variable admittance control for rotational motion in human-robot co-manipulation. *IFAC-PapersOnLine*, 48(19):124–129, 2015.

[34] Brian C Becker, Robert A MacLachlan, and Cameron N Riviere. State estimation and feedforward tremor suppression for a handheld micromanipulator with a kalman filter. In *2011 IEEE/RSJ International Conference on Intelligent Robots and Systems*, pages 5160–5165. IEEE, 2011.

[35] Wei Tech Ang, Pradeep K Khosla, and Cameron N Riviere. Kalman filtering for real-time orientation tracking of handheld microsurgical instrument. In *2004 IEEE/RSJ*

International Conference on Intelligent Robots and Systems (IROS)(IEEE Cat. No. 04CH37566), volume 3, pages 2574–2580. IEEE, 2004.

[36] Günther Deuschl, Peter Bain, Mitchell Brin, and Ad Hoc Scientific Committee. Consensus statement of the movement disorder society on tremor. *Movement Disorders*, 13(S3):2–23, 1998.

[37] Susan L Murphey and Andy Milkowski. Surface emg evaluation of sonographer scanning postures. *Journal of Diagnostic Medical Sonography*, 22(5):298–305, 2006.

Vita

Kevin Gilboy received his Bachelor's in Computer Engineering with a minor in Bioengineering from the University of Pittsburgh in 2018. He began his Master's Degree in Electrical and Computer Engineering at Johns Hopkins University in 2018.

Kevin's research interests include medical robotics and devices, and he generally enjoys working on embedded systems requiring real-time control. He joined both the MUSIIC and CIIS labs at Johns Hopkins University, and worked closely with collaboratively controlled robots with applications ranging from ultrasound computed tomography to laryngeal surgery.

Following the completion of his degree, Kevin will be working as a Robotics Engineer in the R&D Leadership Development Program at DePuy Synthes, a Johnson and Johnson subsidiary, in Boston, MA. There, Kevin will join a team in developing the next generation of orthopaedic surgery robots and devices.